

The moving mesh code SHADOWFAX

B. Vandenbroucke^{a,*}, S. De Rijcke^a

^a*Dept. Physics & Astronomy, Ghent University, Krijgslaan 281, S9, 9000 Gent, Belgium*

Abstract

We introduce the moving mesh code SHADOWFAX, which can be used to evolve a mixture of gas, subject to the laws of hydrodynamics and gravity, and any collisionless fluid only subject to gravity, such as cold dark matter or stars. The code is written in C++ and its source code is made available to the scientific community under the GNU Affero General Public License. We outline the algorithm and the design of our implementation, and demonstrate its validity through the results of a set of basic test problems, which are also part of the public version. We also compare SHADOWFAX with a number of other publicly available codes using different hydrodynamical integration schemes, illustrating the advantages and disadvantages of the moving mesh technique.

Keywords: methods: numerical, hydrodynamics

1. Introduction

Modern simulations of galaxy formation and evolution crucially depend on an accurate treatment of the hydrodynamics of the interstellar medium (ISM) (Vogelsberger et al., 2014; Schaye et al., 2015). The ISM fuels star formation and is disrupted by stellar feedback, and it is this complex interplay that at least partly governs the observable content of galaxies (Verbeke, Vandenbroucke, and De Rijcke, 2015). If we want to be able to compare simulated galaxies with observations, we need to properly resolve these effects.

Hydrodynamics is also important on smaller scales, when simulating star-forming clouds (Greif et al., 2011; Dobbs, 2015), feedback from a single star (Geen et al., 2015), or even planet formation in a circumstellar disc (Duffell and MacFadyen, 2012). A robust hydrodynamical integration scheme, optionally extended with magnetic fields, self-gravity or radiation transport, is hence an indispensable tool for many astrophysical simulators.

Historically, two major classes of hydrodynamical solvers have been developed : grid based Eulerian techniques (Teysier, 2002; Keppens et al., 2012), and particle-based Lagrangian techniques (Springel, 2005; Price, 2012). Both discretize the fluid as a finite set of fluid elements. In the former, the fluid elements are cells, usually defined through a (hierarchical) Cartesian grid, which have a fixed position in space, but can be allowed to refine or derefine according to the quality of the integration. In the latter, the fluid elements are particles, which move along with the flow, with the hydrodynamics being expressed as inter-particle forces.

It is generally acknowledged that grid based Eulerian techniques are more accurate at solving the equations of hydrodynamics, especially since many particle-based implementations have fundamental difficulties in resolving hydrodynamical instabilities (Agertz et al., 2007). Nonetheless, Lagrangian techniques are widely used to simulate systems with a high dynamic range, like cosmological simulations and simulations of galaxies, since they more naturally concentrate computational resources on regions of interest, and provide a Galilean invariant reference frame.

Recently, a new class of hydrodynamical solvers has been developed, mainly through the work of Springel (2010), which aims to combine the advantages of Eulerian and Lagrangian techniques (see also Duffell and MacFadyen, 2011; Yalinewich, Steinberg, and Sari, 2015). This new technique uses a moving grid to discretize the fluid, and combines an unstructured grid based finite volume integration scheme with the Lagrangian nature of a particle method. We will refer to this method as a *moving mesh technique*.

A number of moving mesh codes are presented in the literature (Springel, 2010; Duffell and MacFadyen, 2011), but only two of them are publicly available : `RICH`¹ (Yalinewich, Steinberg, and Sari, 2015), written in C++, and `FVMHD3D`², written in the parallel object-oriented language `CHARM++` (Gaburov, Johansen, and Levin, 2012).

In this paper, we introduce the new, publicly available moving mesh code SHADOWFAX (the logo of the code is shown in Figure 1). SHADOWFAX is written in C++, and makes ample use of the object-oriented capabilities of the language to provide an easy to extend framework. The code is parallelized for use on distributed memory systems

*Corresponding author

Email addresses: `bert.vandenbroucke@ugent.be`
(B. Vandenbroucke), `sven.derijcke@ugent.be` (S. De Rijcke)

¹ascl:1410.005

²<https://github.com/egaburov/fvmhd3d>



Figure 1: The SHADOWFAX logo.

using the Message Passing Interface (MPI)³, and makes use of the open source BOOST C++ libraries⁴ to extend basic C++ language features. The code supports input and output using the HDF5 library⁵ in a format compatible with the output of GADGET2⁶ (Springel, 2005), GIZMO⁷ (Hopkins, 2015) and SWIFT⁸ (Gonnet et al., 2013). A user friendly compilation process is guaranteed through the use of CMAKE⁹.

The hydrodynamical algorithm implemented in SHADOWFAX is the same as described by Springel (2010), but with an additional per-face slope limiter and flux limiter, and optional alternative approximate Riemann solvers. The gravitational calculation is the same as the tree force calculation in GADGET2 (Springel, 2005), and uses the same relative tree opening criterion and Ewald summation technique for periodic boundary conditions. We have ported this algorithm to an object-oriented version, which makes use of compile-time polymorphism using C++ templates. This ensures a clear separation of the algorithmic details underlying the tree walk from the actual physics involved with the gravitational calculation. This way, it is much easier to focus on one particular aspect of the code, e.g. scalability, precision..., without needing to worry about other aspects.

Likewise, we have separated the geometrical details contained in the moving mesh from the hydrodynamical integration as much as possible, to make it easier to replace parts of the algorithm (e.g. the Riemann solver, the grid...) by simply implementing an alternative class.

Our code is predominantly meant to be used in astrophysical simulations of galaxy formation and evolution, but could have applications in other areas of science as well, as it is not difficult to replace the Euler equations of hydrodynamics by e.g. the shallow water equations by implementing a different Riemann solver. Furthermore, the Voronoi grid used to discretize the fluid can also be used for other purposes, e.g. for the suppression of Poisson noise in randomly sampled distributions through Lloyd's

algorithm (Lloyd, 1982), or as density estimator in N-body simulations (Cloet-Osselaer et al., 2014).

In this paper, we outline the basic working of SHADOWFAX. We mainly focus on the C++ implementation and the object-oriented design of our code, and compare our code with other hydrodynamical solvers on a number of test problems. Although the current version of SHADOWFAX focusses more on design and accuracy than on performance, we also highlight some basic strong and weak scaling tests. Performance optimizations and extra physical ingredients (e.g. gas cooling, star formation and stellar feedback...) will be added in future versions of the code. The source code of SHADOWFAX is publicly available from <https://github.com/AstroUGent/shadowfax>, and is distributed under the GNU Affero General Public License¹⁰.

2. Algorithm

Many of the algorithms implemented in SHADOWFAX were already discussed in Springel (2005) and Springel (2010). For completeness, we summarize them below and point out the differences where necessary.

SHADOWFAX is based on a finite volume method, which subdivides the computational box into a (large) number of small cells. The hydrodynamical integration is governed by the exchange of fluxes between these cells.

These fluxes involve the *conserved variables* : mass (m), momentum (\mathbf{p}) and total energy (E). The Euler equations of hydrodynamics however are usually formulated in terms of *primitive variables*: density (ρ), flow velocity (\mathbf{v}) and pressure (p). The pressure is sometimes replaced by the thermal energy (u) or some form of entropic function of the fluid, by using the *equation of state* of the fluid. In this work, we will always assume an ideal gas, with an equation of state of the form

$$p = (\gamma - 1)\rho u, \quad (1)$$

where γ is the *adiabatic index* of the gas, for which we will adopt the value $\gamma = 5/3$, unless otherwise stated. The conserved variables and primitive variables can be converted into one another whenever a volume (V) is available, since

$$m = \rho V \quad (2)$$

$$\mathbf{p} = m\mathbf{v} \quad (3)$$

$$E = mu + \frac{1}{2}m\mathbf{v}^2. \quad (4)$$

It is common practice to combine the conserved and primitive variables into two *state vectors*,

$$\mathbf{Q} = \begin{pmatrix} m \\ \mathbf{p} \\ E \end{pmatrix} \quad \text{and} \quad \mathbf{W} = \begin{pmatrix} \rho \\ \mathbf{v} \\ p \end{pmatrix}. \quad (5)$$

³<http://www.mpi-forum.org>

⁴<http://www.boost.org>

⁵<https://www.hdfgroup.org/HDF5>

⁶ascl:0003.001

⁷ascl:1410.003

⁸<http://icc.dur.ac.uk/swift/>

⁹<https://cmake.org>

¹⁰<http://www.gnu.org/licenses>

The change in conserved variables \mathbf{Q}_i for a cell i , during an integration time step of length Δt , is then given by

$$\Delta \mathbf{Q}_i = -\Delta t \sum_j A_{ij} \mathbf{F}_{ij}(\mathbf{W}_i, \mathbf{W}_j, \nabla \mathbf{W}_i, \nabla \mathbf{W}_j, \mathbf{v}_{ij}, \Delta t), \quad (6)$$

where A_{ij} is the surface area of the interface between cell i and cell j . \mathbf{F}_{ij} is the flux between cell i and cell j , which in general depends on the primitive variables of both cells and their gradients, the velocity \mathbf{v}_{ij} of the face with respect to a frame of reference fixed to the simulation box, and the integration time step.

When formulated in this way, the finite volume method can be applied to any discretization of the fluid, as long as this discretization yields volumes to convert conserved variables to primitive variables, and defines a concept of neighbour relations between cells, and an associated surface area and velocity for the neighbour interface. It can even be applied to mesh-free, particle-based methods (Hopkins, 2015).

In the case of a moving mesh method, the discretization is given by an unstructured Voronoi mesh, a 2D example of which is shown in Figure 2. The mesh is defined by means of a set of mesh generating points (*generators*), with the cell associated with a specific generator containing the region of space closest to that generator. A Voronoi mesh can be defined in D dimensions, but we will focus on the cases $D = 2$ and $D = 3$. The Voronoi mesh has the interesting property that it is relatively stable under small movements of the generators (Reem, 2011), so that cells deform continuously under a continuous movement of the generators. We exploit this property to allow the mesh to move in between integration time steps. The surface area of the faces will change linearly in between steps, so that the time averaged flux over the entire time step will be correct, even if it is calculated at one specific moment in time.

By setting the velocities of the mesh generators equal to the local flow velocity, the mesh will effectively move along with the fluid, and we end up with a Lagrangian method. We can even reinterpret the generators as being particles, so that the moving mesh technique becomes a true alternative for particle-based methods. However, the underlying integration scheme uses the full strength of a finite volume method, and hence will be more accurate. Note that the quality of the integration will depend on the shape of the cells, with highly irregular cells leading to less accuracy (Vogelsberger et al., 2012). To ensure cell regularity, it is sometimes necessary to add extra correction terms to the generator velocities. We employ the scheme of Springel (2010) and steer the cell generator towards the centroid of its cell if the distance between generator position and cell centroid exceeds a fraction of the generic cell size, i.e. the radius of a sphere with the same volume as the cell.

In the remainder of this section, we describe the mesh

construction and flux calculation in more detail, to introduce the concepts that are used in the discussion of the SHADOWFAX implementation.

2.1. Mesh construction

We construct the Voronoi mesh through its dual Delaunay triangulation. The latter is constructed using an incremental construction algorithm. In the default implementation, the relevant parts of the mesh are reconstructed for every time step. We also experimented with a mesh evolution algorithm (Vandenbroucke & De Rijcke, in preparation), which evolves the mesh instead of reconstructing it.

As Richard Shewchuk (1997) pointed out, incremental Delaunay construction algorithms can become unstable due to numerical round-off error. To prevent this from happening, we employ arbitrary exact arithmetics for all geometrical tests involved. Since the predicates of Richard Shewchuk (1997) depend on a number of assumptions on the internal CPU precision that are not met on all hardware architectures, we use the technique outlined by Springel (2010) : we map the floating point coordinates of the mesh generators to the interval $[1, 2]$ and use an integer representation of the mantissa to exactly calculate the result of a geometrical test if the numerical error could lead to a wrong result. We pre-calculated the maximal size of an integer necessary to store the exact result and use the BOOST MULTIPRECISION library¹¹ to perform the calculations using long integer arithmetics.

The result of the mesh construction is a list of neighbours for every mesh generator, and an associated list of faces, with each face consisting of an ordered list of vertex positions. We need to compute the volume and geometrical centroid of each cell from this, as well as the surface area and midpoint of every face.

In 2D, the faces each contain only two vertices, with the midpoints being the midpoints of the line segments formed by these two vertices. In this case, we order the neighbours and faces counter-clockwise around the position of the generator of the cell. The volume (2D surface area) of the cell is then given by the sum of the surface areas of the triangles that are formed by the first vertex and two consecutive other vertices. The centroid of the cell is then the weighted average of the centroids of these same triangles.

In 3D, we use a similar technique to obtain the surface area and midpoint of the individual faces. The total volume of the cell is then the sum of the volumes of the pyramids with the faces as base and the cell generator as top (the latter being guaranteed to lie inside the cell). The centroid is the weighted average of the centroids of these pyramids.

The mesh construction algorithm only works if all cells, including those at the borders of the simulation volume,

¹¹<http://www.boost.org/doc/libs/release/libs/multiprecision/>

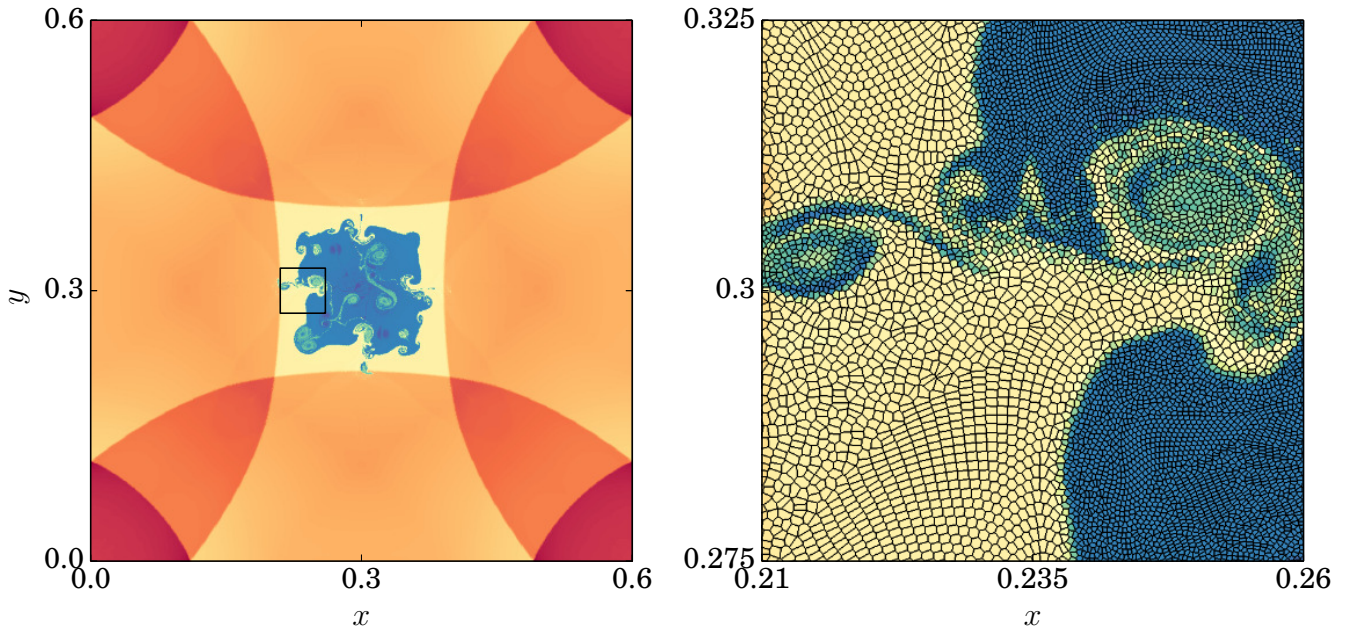


Figure 2: Density colour plot for the 2D Liska and Wendroff (2003) implosion test at $t = 0.5$. *Left*: general view of the entire simulation box, *right*: zoom in on part of the central low density region. The Voronoi mesh used for the discretization of the gas has been overplotted.

have boundaries. To make sure this is the case, we always enclose all generators in a simulation box, which is a cuboid. Cells at the boundaries are then completed by inserting ghost generators. If we want periodic boundaries, we insert periodic copies of generators at the other side of the simulation box. We can also mirror the generator positions themselves with respect to the boundary face of the simulation box, in this case we have reflective boundaries.

During the flux calculation, these ghost generators then either represent the cell of which they are a periodic copy, or the border cell itself, but with the sign of the flow velocity along the boundary face normal reversed.

2.2. Flux calculation

We employ a Monotonic Upwind Scheme for Conservation Laws (MUSCL) combined with a Hancock prediction step to estimate the fluxes. This scheme is more commonly referred to as a MUSCL-Hancock scheme. The flux calculation consists of a cell based interpolation and integration step, whereby the primitive variables at the center of the cell (the centroid of the Voronoi cell) are interpolated to the position of the midpoint of the face using the gradients of the primitive variables in that cell, and are predicted forward in time for half the time step using the same gradients and the Euler equations in primitive form.

These face reconstructed primitive variables are then used as the input for a Riemann solver, to obtain appropriately averaged primitive quantities at the interface which take into account the local wave structure of the Euler equations (Toro, 2009). This can be done using either an

exact, iterative Riemann solver, or an approximate Riemann solver. The solution of the Riemann problem, \mathbf{W}_* , is then used to calculate the hydrodynamical fluxes as

$$\mathbf{F}(\mathbf{W}_*) = \begin{pmatrix} \rho_* \mathbf{v}_* \\ \rho_* \mathbf{v}_* \mathbf{v}_* + p_* \\ \rho_* (u_* + \frac{1}{2} \mathbf{v}_*^2) \mathbf{v}_* + p_* \mathbf{v}_* \end{pmatrix}. \quad (7)$$

The Riemann problem is generally formulated in 1D, with the change in variables corresponding to a change in x coordinate. In an unstructured mesh, the face normals are generally not aligned with the x axis, so that we need to rotate the primitive variables to a reference frame where the x axis is aligned with the surface normal of the face. This only affects the fluid velocity components. The solution of the Riemann problem then needs to be rotated back to the original reference frame.

When the cells are allowed to move, the faces will move as well, and we need to transform to a frame of reference moving along with the face before solving the Riemann problem. This again only affects the fluid velocity components of the primitive variables.

However, the flux needs to be adapted in this case as well : even if the hydrodynamical flux through the face would normally be zero, there will be net flux, caused only by the movement of the cell. This flux is given by

$$\mathbf{F}_{\text{mov}}(\mathbf{W}_*) = - \begin{pmatrix} \rho_* \mathbf{v}_{ij} \\ \rho_* \mathbf{v}_* \mathbf{v}_{ij} \\ \rho_* (u_* + \frac{1}{2} \mathbf{v}_*^2) \mathbf{v}_{ij} \end{pmatrix}. \quad (8)$$

We can either add this correction flux to the hydrodynamical flux (Springel, 2010), or calculate the hydrodynamical flux in a reference frame moving along with the face and correct for the movement afterwards (Pakmor, Bauer, and Springel, 2011).

2.3. Limiters

A side effect of the gradient interpolation step discussed above is the possible introduction of new extrema of the primitive variables, which can cause spurious oscillations in the solution (Toro, 2009). These spurious oscillations can be avoided by constructing monotone schemes, whereby the gradients of a cell are limited so that no interpolated primitive value can exceed the primitive variables in one of the neighbouring cells. However, such monotone schemes are no longer second order accurate in space, so that a limiting procedure inevitably leads to a loss of accuracy. It might therefore be better to use a somewhat less restrictive gradient limiter, as long as the spurious oscillations do not dominate the local solution (Hopkins, 2015). We use the cell wide slope limiter described by Springel (2010).

Apart from a cell wide slope limiting procedure that limits the gradients of the cell during the gradient calculation (which is performed after the primitive variables have been calculated, but before the fluxes are computed), it is also possible to limit the interpolated values at the faces. The general idea of such a pair-wise slope limiter is to conserve the wave structure of the Riemann problem. This wave structure generally consists of a central contact discontinuity and a left and right wave, which can be either a shock wave or a rarefaction wave (Toro, 2009). Spurious oscillations arise when the solution of the Riemann problem with the cell centered primitive variables as input yields e.g. a left and right rarefaction wave, while the Riemann problem with the interpolated variables at the face yields a left shock wave and a right rarefaction wave. The left shock is not present in the first order solution, and introduces a growing artefact in the solution. With a pair-wise limiter, we limit the left and right interpolated values in such a way that the original wave structure of the Riemann problem is the same, but the input values can still differ from the cell centred values. We implemented the pair-wise slope limiter of Hopkins (2015).

Even with appropriate slope limiters, it is still possible that the calculated fluxes are too large, i.e. exceed the value of the conserved variables in the cell. For the mass and energy of the cell, this is fatal, since this can cause negative masses and energies, which are evidently unphysical. This can happen for example if the integration time step is too large, if the gradient interpolation is done in an asymmetric way (due to pair-wise limiting), or if external forces (e.g. gravity) contribute to the flux. The former is normally excluded by choosing an appropriate time step criterion. To prevent the latter from crashing the code, we implemented a *flux limiter*, which ensures that the flux through a face can never be larger than a fraction of the

value of the conserved variables inside the cell. This fraction is equal to the ratio of the surface area of the face to the total surface area of the entire cell.

We note that a flux limiter is only used to ensure code stability, and in this sense is equal to resetting the mass or energy of a cell to some very small value whenever they become negative. However, by limiting the flux and not the cell quantities themselves, we ensure manifest conservation of mass and energy, which would otherwise be violated.

2.4. Gravity

Gravity is added as an extra term in the momentum equation:

$$\Delta \mathbf{p}_i = -\Delta t \sum_j A_{ij} \mathbf{F}_{ij,p} - \frac{1}{2} \Delta t (m_{i,\text{old}} \nabla_i \Phi_{\text{old}} + m_{i,\text{new}} \nabla_i \Phi_{\text{new}}), \quad (9)$$

where $m_{i,\text{old}}$ and $m_{i,\text{new}}$ represent the mass inside the cell before and after the update of the mass respectively, and $\nabla_i \Phi_{\text{old}}$ and $\nabla_i \Phi_{\text{new}}$ represent the gravitational acceleration before and after the generator positions have been updated. $\mathbf{F}_{ij,p}$ is the hydrodynamical flux for the momentum, as given above.

The gravitational acceleration is also taken into account during the half step prediction, before the flux calculation, and only affects the velocity.

Gravity also affects the total energy of the cell. Simply adding a term to the energy equation does not take into account the movement of the mass that fluxes through cell faces during the time step, and leads to significant energy errors. We therefore use the following more involved equation to update the energy of a cell:

$$\Delta E_i = -\Delta t \sum_j A_{ij} \mathbf{F}_{ij,E} - \frac{1}{2} (m_{i,\text{old}} \mathbf{w}_{i,\text{old}} \nabla_i \Phi_{\text{old}} + m_{i,\text{new}} \mathbf{w}_{i,\text{new}} \nabla_i \Phi_{\text{new}}) - \frac{1}{4} \sum_j \Delta m_{ij} (\mathbf{r}_i - \mathbf{r}_j) (\nabla_i \Phi_{\text{old}} + \nabla_i \Phi_{\text{new}}), \quad (10)$$

where $\mathbf{w}_{i,\text{old}}$ and $\mathbf{w}_{i,\text{new}}$ represent the generator velocities before and after the update of the generator positions, and Δm_{ij} is the mass that fluxed from cell i to cell j during the time step. The sum extends over all neighbours of the cell.

We soften the gravitational acceleration for both the hydrodynamical and collisionless component using a spline kernel with fixed softening length (Springel, 2005). A gravitational time step criterion based on the size of the gravitational acceleration and the softening length is combined with the hydrodynamical time step criterion to set the particle time steps.

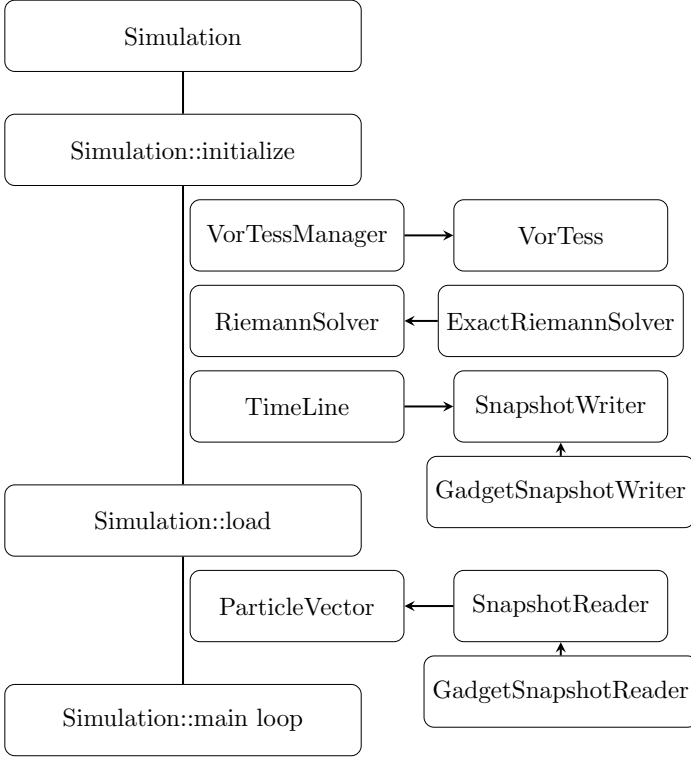


Figure 3: General overview of a simulation, using the default Voronoi mesh, Riemann solver and input/output classes. After the desired implementations of the main classes have been constructed during an initialization step, the initial conditions are read in and stored in a `ParticleVector` data structure that will be updated during the main simulation loop.

3. Implementation

The finite volume method and the actual discretization of the fluid as a Voronoi mesh are clearly well separated concepts, so that it makes sense to separate them in the design of a moving mesh code. It then becomes possible to test the finite volume method using e.g. a fixed Cartesian mesh, which is computationally much cheaper to construct, or to treat the mesh generators as particles and calculate volumes and interfaces using a mesh-free method (Hopkins, 2015).

Furthermore, various parts of the finite volume method can be adapted, and could be considered to be run time parameters for the code: the choice of Riemann solver, the choice of slope limiter,... A good code design should make it possible to easily exchange these components without affecting other parts of the algorithm, and where possible also without the need to recompile the code.

Figure 3 shows a general overview of a simulation, as it is implemented in the `Simulation` class, introducing the main classes of interest. Figure 4 shows how these different classes interact during the main simulation loop.

In this section, we describe how various aspects of the algorithm were implemented in the public version of SHADOWFAX. We highlight important abstractions, but also indicate where our current version does not comply with the

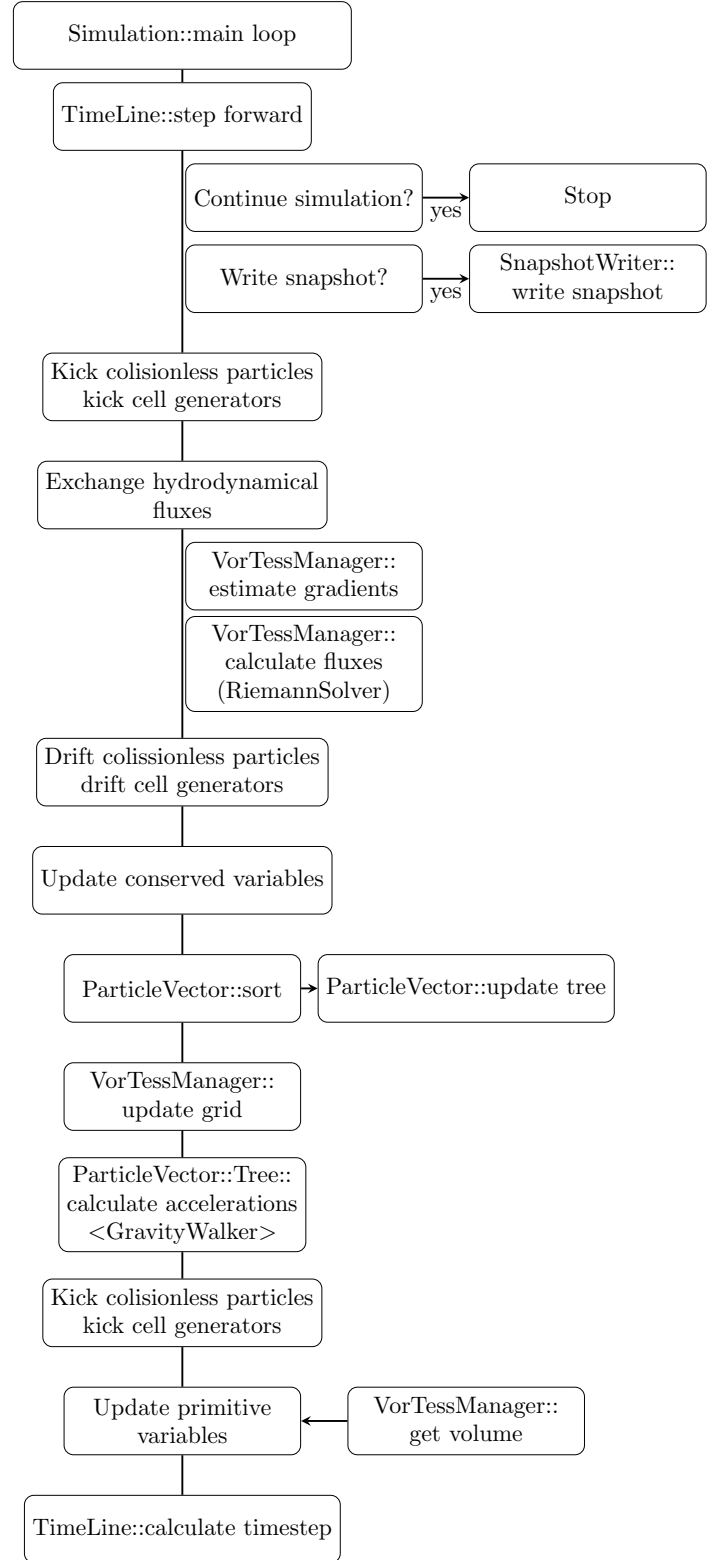


Figure 4: Overview of the main simulation loop. We combine a leapfrog integration for the gravitational force with a simple kick-drift scheme for the hydrodynamics. Geometrical properties like cell volumes, neighbour relations and face properties are extracted from the `VorTessManager`, gravitational forces are calculated using the `Tree` managed by the `ParticleVector`, using a template `GravityWalker`. All time related stuff is handled by the `TimeLine`.

high standards formulated above. This is mainly caused by the way in which the code was developed historically, and changing them will be subject of future work for versions of the code to come.

We also discuss the parts of the code that are not related to the hydrodynamical integration, like the gravity calculation, which makes use of advanced C++ language features to increase the readability and abstraction level of the code. The input and output for initial conditions, parameters, snapshot files and restart files are discussed as well.

3.1. Voronoi mesh and hydrodynamics

We have isolated the Voronoi mesh in a **VorTessManager** class, which encapsulates the entire mesh into a single object. Particles can be added to the **VorTessManager** as a pair consisting of a set of coordinates and an integer key, so that the properties of the cell or mesh-free particle can then later be retrieved by means of that same key. The **VorTessManager** itself decides how these properties are calculated. This can be either by using a Voronoi mesh, by using a fixed Cartesian grid, or even by using a mesh-free method. The Voronoi mesh could be constructed from the positions of the particles, but it can also be evolved from the Voronoi mesh from a previous time step. The public version of SHADOWFAX for the moment only contains the ordinary (non-evolved) Voronoi mesh and the fixed Cartesian grid. The evolving mesh will be added as part of future work (Vandenbroucke & De Rijcke, in preparation).

The fluxes are calculated through faces, which could in principle be returned by the **VorTessManager** as **VorFace** objects, which contain the surface area and midpoint of the face, as well as the indices of the two neighbouring generators. However, due to the historical development of the code and the complexities involved with parallelizing the Voronoi mesh, the flux calculation is implemented as a method of the **VorTessManager** object for the moment, with the entire interpolation, integration and flux estimation procedure being implemented as a method of the **VorFace** object.

3.1.1. Voronoi mesh

The ordinary Voronoi mesh is contained in a **VorTess** object, which contains an actual list of the faces and of the cells, represented as **VorCell** objects. The **VorCell** object contains the necessary methods to calculate volumes and centroids, and in the current version of the code also the methods that estimate the gradients and calculate the generator velocities.

When adding a particle to the **VorTess**, the particle coordinates are mapped to the range $[1, 2]$ and stored in a **VorGen** object, which represents a mesh generator. This object is stored in a **DelTess** object, which represents the Delaunay triangulation. The **DelTess** object also contains a list of **Simplex** objects, which represent the 2D triangles or 3D tetrahedra that constitute the triangulation. Each

Simplex object has 3 or 4 **VorGen** objects as vertices (depending on the dimension). During the incremental construction algorithm, these simplices will change. When all particles have been added to the **VorTess** object, we call an appropriate method to signal this. At this point, a method of the **DelTess** object is called that will ensure completeness of the Delaunay triangulation (by adding inactive particles that are neighbour to active particles, and ghost generators for particles on other MPI processes). When this is done, the actual Voronoi mesh is constructed by looping over the **VorGen** objects stored in the **DelTess** and adding a **VorCell** for every **VorGen**. For every neighbour relation between **VorGens**, a **VorFace** is created. At the end of the procedure, we also calculate the volumes, centroids, surface areas and midpoints of all cells and faces.

3.1.2. Riemann solvers

When the flux calculation method of the **VorTessManager** object is called, we pass on a general **RiemannSolver** object, which is used to solve the Riemann problem at the faces, but also to convert between primitive and conserved variables, and to calculate the actual fluxes. The **RiemannSolver** class itself is just an interface, with the actual implementation being deferred to child objects. The public version of SHADOWFAX implements two Riemann solvers : an exact Riemann solver (**ExactRiemannSolver** class), and a two rarefaction Riemann solver (**TRRSSolver** class), which is an approximate solver that assumes a wave structure containing two rarefaction waves.

Which Riemann solver is used, is specified as a run time parameter. To generate the appropriate **RiemannSolver** implementation, a **RiemannSolverFactory** class is used, which implements methods that convert a string representation of a Riemann solver type to an object. A single **RiemannSolver** object is created during program initialization and used throughout the simulation, so that the **RiemannSolver** can store some valuable information about the number of Riemann solver evaluations and the fraction of the run time spent in Riemann solver evaluations.

Since the Riemann solver contains all information about the actual equations being solved, it is possible to experiment with new equations of state by writing new **RiemannSolver** implementations.

For all tests presented in this paper, we use the exact Riemann solver.

3.2. Time line and snapshots

Apart from the spatial discretization, the system of equations is also discretized in time. We have implemented an individual time stepping scheme, in which cell time steps are power of 2 subdivisions of the total simulation time. Fluxes are always exchanged using the smallest time step of the two cells involved, and the time step of a cell can only increase again if it then becomes synchronized with other cells on the same time step level. The system is always evolved using the smallest time step of all cells,

but only those cells that are active at the beginning of the current system time step are actually integrated.

The size of the time step depends on the hydrodynamics and hence should ideally be set in the **RiemannSolver** class. However, for problems involving gravity, there is also a gravitational time step criterion. Furthermore, the size of the time step is also governed by a stability parameter (called the Courant-Friedrichs-Lewy or CFL parameter), which is specified as a run time parameter for the program. We hence have opted to make the time step calculation a method of a **TimeLine** object, which takes both the hydrodynamical time step criterion and the gravitational time step criterion into account and applies the correct CFL parameter. To separate the hydrodynamical aspects, all hydrodynamically relevant information is encoded in two velocities : the fluid velocity and a sound speed, which is calculated by a method of the **RiemannSolver** object.

We also implemented an advanced, tree walk based time step criterion to adapt the cell time step in the presence of strong shocks. This criterion makes use of the template tree walks discussed below. However, for simulations involving regular flow and a high dynamic range, this criterion was found to be very expensive, so that we disable this criterion by default. This criterion can be activated by setting the corresponding run time parameter.

The **TimeLine** object also keeps track of the system time, and provides methods to convert floating point time values to an internally used integer timeline (which is more convenient when using a power of 2 time step hierarchy). The **TimeLine** is also responsible for writing snapshot files.

Snapshots are dumps of the positions and primitive variables of the particles (along with other relevant quantities) at a particular system time. The time interval in between snapshots can be specified as a run time parameter and is stored in the **TimeLine**, together with a counter that keeps track of the number of snapshot files already written. Whenever the system time becomes equal to or larger than the time for the next snapshot, a signal is sent to an implementation of the **SnapshotWriter** interface, which is responsible for writing the snapshot. Note that this means that snapshots are not necessarily written at the exact time requested, if that time does not coincide with an actual system time. This is a consequence of our strict power of 2 time step hierarchy and the fact that we do not drift quantities in between system times. Usually however, the difference will be small. Note also that the use of individual time steps means that not necessarily all cells will be active at the time when a snapshot is written. In this case, the primitive variables that were calculated at the last point in time when a cell was active are used for that cell. Again, the difference will usually be small.

The **SnapshotWriter** interface defines a method that writes the actual snapshot. Two implementations are provided : **ShadowfaxSnapshotWriter**, which writes snapshots in the historically native SHADOWFAX format, and **GadgetSnapshotWriter**, which writes snapshots in the same format that is also used for GIZMO and SWIFT, and was one

of the possible snapshot formats for GADGET2. Both formats are based on the HDF5 file format.

Initial condition files have the same format as snapshot files, and are read in using the appropriate implementation of the **SnapshotReader** interface. Both the format of the initial conditions as that of the snapshot files can be specified as a run time parameters for the program, the default format being the GADGET format. Appropriate objects are generated using the **SnapshotReaderFactory** and **SnapshotWriterFactory** classes.

3.3. Tree algorithms

Gravitational accelerations are calculated using a Barnes-Hut tree walk (Barnes and Hut, 1986), using a relative tree opening criterion (Springel, 2005). To this end, a hierarchical octree is constructed : a **Tree** object. This object holds a pointer to a single implementation of the **Node** interface, which is called the root of the tree. The **Node** interface has two implementations, **TreeNode** and **Leaf**, which correspond to respectively a node and a leaf of the octree. Each **TreeNode** has up to 4 or 8 children (depending on the dimension), which themselves are also **Node** implementations, and can be either a **TreeNode** or a **Leaf**. Each **Leaf** holds a pointer to a single **Particle**, which can be either a **GasParticle** or a **DMParticle** (see below). In parallel simulations, there is also a third type of **Node**, called a **PseudoNode**, which is used to represent a **TreeNode** on another MPI process.

The tree is constructed using an incremental construction algorithm, and making use of the close link between the levels of the tree and the levels of a Hilbert space filling curve (Sundar et al., 2008), the latter also being used for the domain decomposition (Springel, 2005). To this end, we first calculate a Hilbert key for each particle, using the efficient algorithm of Jin and Mellor-Crummey (2005). We use a global octree on each process, with nodes that are entirely on other processes being represented by pseudo nodes.

The gravitational tree walk itself is in essence the same as in GADGET2, using the same Barnes-Hut tree algorithm with relative opening criterion and Ewald summation to treat periodic boundaries, but it has been entirely rewritten to increase readability and code reuse. To this end, we have defined a general **TreeWalker** interface. Every tree walk, be it a tree walk to obtain gravitational accelerations, or a tree walk to find the neighbours of a particle within a given radius, is then represented by an implementation of this interface. The interface itself defines methods that correspond to the different tasks during a tree walk : a method to check whether a node of the tree should be opened or treated approximately, a method called when a leaf is encountered, and a method that is called when a pseudo node is encountered and checks whether the tree walk should be continued on another process. Apart from this, the interface also defines methods that initialize the variables used during the tree walk, and a method that is called when the tree walk is finished.

Every possible tree walk is implemented as a single method of the `Tree` class, using the concept of C++ templates. To this end, the tree walk method takes the name of a `TreeWalker` implementation as a template argument, as well as a list of particles for which the tree walk should be performed. For every particle in the list, a corresponding `TreeWalker` object is created and used to walk the tree : we open the root node of the tree and apply the method that checks if a node should be opened on its children. If a node should be opened, we continue with its children, if not, we execute all calculations that are necessary to get the approximate contribution of the entire node to the tree walk, using the node properties. If a leaf is encountered, the properties of the corresponding particle are used, and we continue with the next node or leaf on the same level.

By using class methods to define the different steps in the tree walk, the code is a lot easier to read, since, for instance, the code that decides if a node should be opened now is in a separate method that takes a `TreeNode` as single parameter. We do not need to worry about how to implement the tree walk itself efficiently, only about what happens when a node or leaf is encountered. By using C++ templates, we limit the overhead usually involved with run time polymorphism, since the code for a specific type of `TreeWalker` is generated at compile time.

Our approach has some benefits for MPI parallelization as well, since all explicit communication (and the design of an effective communication scheme) is limited to the single tree walk method. The only tree walk specific things we need to do, are deciding if communication is necessary (which is in most cases similar to deciding whether or not to open a node), deciding what information to communicate, and how the result of the tree walk on another process should be communicated back to the original process. To this end, our `TreeNode` interface defines two subclasses, called `Export` and `Import`.

3.4. Particles

The different physical components of the simulation are all represented by `Particles`, which is an abstract class holding a position and velocity, as well as an unique identifier (ID), which can be used to trace a single particle throughout different snapshots. Currently, two subtypes of `Particle` are supported : `GasParticles` and `DMParticles`, representing the generators of the Voronoi mesh and a collisionless cold dark matter component respectively. We have adopted the name `GasParticle` instead of `cell` to reflect the fact that our hydrodynamical method is just an alternative for common particle-based hydrodynamical integration schemes. For the gravitational calculation, the gas is treated as if it consists of particles.

The `GasParticle` class extends the particle data with two `StateVector` members, representing the primitive and the conserved quantities for that cell. It also holds a number of other variables required by the hydrodynamical integration scheme. The `DMParticle` only holds a particle

mass and some auxiliary variables for the gravitational calculation.

The `Particle` class itself extends the `Hilbert_Object` interface, which links a space filling Hilbert key to it. Every class that implements the `Hilbert_Object` interface can be sorted using an efficient `ParallelSorter`, based on Siebert and Wolf (2010). The `ParallelSorter` takes care of the domain decomposition and data size based load-balancing across all MPI processes. The domain decomposition is currently only based on the number of particles, and tries to assign equal numbers to all processes. This simple approach only works for homogeneous setups with small numbers of processes, and will be replaced by a more advanced cost-based domain decomposition in future versions of the code.

`Particles` of all types are stored in a `ParticleVector`, which is a specialized wrapper around two standard C++ `vector` objects. The class has member methods to separately access `Particles` of both types, and is also responsible for maintaining the `Tree` and storing some general information about the simulation.

3.5. Units

We have adopted the strategy used by SWIFT, and force all quantities that are used as input or output of our program to have units attached to them. To this end, both snapshot formats have appropriate blocks specifying in what units the given data are expressed, given in terms of a reference unit system, which is either the SI or CGS system. If no units are specified for the initial condition file, SI units are assumed by default. The output units can be chosen as a run time parameter, as well as the internally used units. Run time parameters that should have units are assumed to be in internal units, the default being SI units.

In principle, it does not matter what units are used internally in our code, although using a system of units in which variables have values close to unity can be advantageous. Furthermore, all run time log information will be expressed in internal units, so that it is useful to have some idea of what units are used.

To simplify working with units, we have implemented a `Unit` class. This class stores the quantity for which the unit is used, expressed as a combination of the three basic quantities *length*, *mass* and *time*, and the value of the unit in SI units. *Temperature* and *current* should be added to the set of basic quantities to be able to express all possible quantities, but these are not used for the variables that are currently evolved in SHADOWFAX.

Units can be multiplied with or divided by one another, yielding a new `Unit`. To make working with quantities in this case possible, we have adopted some conventions of how quantities should be combined. We also made it possible to compare different `Units`, with two `Units` being compatible if their quantities are equal. Quantities with compatible `Units` can be converted into each other by using a `UnitConverter`. A combination of a length, mass and

time unit defines a complete unit system, a **UnitSet**, which is what we specify as a run time parameter for the program. We currently support three different unit systems : SI units (m, kg, s), CGS units (cm, g, s) and galactic units (kpc, M_{\odot} , Gyr), which can be generated using the **UnitSetGenerator** class.

Physical constants also have units, but usually their value is fixed. We have hard coded the values of relevant physical constants (currently only the gravitational constant $G = 6.67408 \times 10^{-11} \text{ m}^3 \text{ kg}^{-1} \text{ s}^{-2}$) in SI units, and store their value in internal units in a **Physics** object. We have provided a mechanism to override the physical value of the gravitational constant at run time for test purposes, but there are no plans to generalize this approach for other physical constants.

3.6. Restarting

Since SHADOWFAX is meant to be used on small clusters for simulations that take several days or even weeks to complete, we need to address the possibility that runs might be interrupted, either by limits on the use of infrastructure, or by hardware failure. Since the initial condition files and snapshot files have the same format, it is always possible to restart a run from the last snapshot. However, since a snapshot is not necessarily written at a time when all cells are active, this will affect the outcome of the simulation.

We therefore implemented an explicit restart mechanism that dumps the entire simulation to binary files and then restarts it as if the run never stopped. This is represented by a **RestartFile** object. This object has two template methods, **write** and **read**, with several specializations, to write values in all sorts of formats to the binary file without the need to explicitly type cast anything. All objects in the simulation that need to be dumped to the restart file either implement a **dump** method, which writes member variables to the restart file, or are written entirely to the restart file using one of the **write** specializations.

When restarting the run, objects are either created using a special constructor which initializes values by reading them from the restart file, or are read entirely from the file using an appropriate **read** specialization. To ensure a proper working of the restart mechanism, we only need to make sure that values are written and read in the same order.

Since restarting a run is only meant to be done when the run was somehow interrupted, the **RestartFile** also writes a short summary file, containing compilation, run time and version information about the program that created the dump. When restarting, this file is read in and the information is compared with the running program. Only when the same version of the code, with the same compilation time and the same run time environment is used, do we allow the code to restart.

3.7. Future improvements

The current version of the code still contains traces of the way in which it was originally developed, that do not comply with our strict design goals. However, refactoring the code to eliminate these infers a major update, and is postponed to a future version of the code. We give a brief overview below.

- **VorFace** still contains the entire gradient reconstruction and prediction step, as well as the flux calculation. These should be isolated into a new class that use the properties of the **VorFace**, but can be decoupled from its geometric meaning.
- Similarly, **VorCell** still contains the gradient estimation and the generator velocity calculation. These should be calculated inside a new class that uses the **VorCell** properties.
- Currently, only the time step tree walk and the gravitational tree walk use a template **TreeWalker**, the neighbour search is still hardcoded in the **Tree** class.
- The MPI communication for the cells is strongly coupled to ghost **VorGens** stored in the **DelTess**. As a result, all cell communication has to go through the **VorTessManager**, which is not ideal.
- The domain decomposition does not take into account the effective computational cost on an MPI process, but is only based on particle number.
- The **FixedGrid** only works if the particles have specific positions and do not change their positions. This means the **VorTessManager** should have control over the positions of the particles, and no other class.

4. Setup and analysis

Apart from the main simulation program, the public release of SHADOWFAX also includes two auxiliary programs that can be used to generate initial condition files, and to convert snapshot files to VTK files that can be easily visualized using common visualization packages. These are discussed below.

4.1. Initial condition generation

Since the default file format for SHADOWFAX is the same as for a number of important other astrophysical codes, it is possible to use software written for those codes to generate initial conditions for SHADOWFAX, or to analyse SHADOWFAX results. We however also provide our own initial condition generating software, which is a part of SHADOWFAX. It is also worth noting that HDF5 has a user-friendly Python interface, **h5py**¹².

¹²<http://www.h5py.org>

Our own program is called `icmakerXd`, (with **X** being 2 or 3), and is based on the initial condition mechanism implemented in the AMR code `RAMSES`¹³ (Teyssier, 2002). The simulation box is divided into a number of geometrical *regions*, each having a geometrical shape and values for the primitive hydrodynamical variables inside that region. Multiple regions can overlap, in this case the values for the region that was last added are used in the overlap region.

The shape of the region is set by defining the position of the origin $\mathbf{o} = (o_x, o_y, o_z)$ of the region, and 3 widths, w_x, w_y, w_z , together with an exponent e . The latter is used to determine if a point $\mathbf{p} = (p_x, p_y, p_z)$ lies inside the region. For this, the inequality

$$\left[\left(2 \frac{o_x - p_x}{w_x} \right)^e + \left(2 \frac{o_y - p_y}{w_y} \right)^e + \left(2 \frac{o_z - p_z}{w_z} \right)^e \right]^{\frac{1}{e}} \leq 1 \quad (11)$$

needs to hold. For 2D setups, we only have 2 widths and the last term drops out of this inequality.

We have extended the `RAMSES` scheme and do not only allow constant values for the primitive variables inside a single region, but also more complex expressions, containing mathematical operations (+, −, ×, /), basic mathematical functions (cos, sin...), mathematical constants (π), and even coordinate expressions (x, y, z and r). Support for these expressions is provided by `BOOST SPIRIT`¹⁴.

`icmakerXd` has support for regular Cartesian setups, but also for random unstructured grids, whereby grid generators are sampled according to the hydrodynamical density of the regions, using rejection sampling. To this end, the (potentially) complex density profiles inside the different regions are numerically integrated to obtain weighing factors. Allowing complex expressions makes this computationally expensive, but makes the program a powerful tool for initial condition generation.

To smoothen out Poisson noise in random generator setups, we apply 10 iterations of Lloyd’s algorithm (Lloyd, 1982). This yields a more regular initial mesh.

4.2. Visualization

Visualizing a Voronoi mesh is not so straightforward, especially in the case of a 3D mesh. Furthermore, the vertices of the Voronoi mesh are not written to the snapshot files, so that the mesh needs to be recalculated if we want to visualize the mesh corresponding to some snapshot file. This requires a Voronoi construction algorithm, and hence we have written an auxiliary program, called `vtkmakerXd` that converts a regular snapshot to a dump of the Voronoi mesh, in the VTK file format¹⁵. This file format can be read by software that makes use of the powerful Visualization Toolkit (VTK), the most commonly used examples being Paraview¹⁶ and VisIt¹⁷.

¹³ascl:1011.007

¹⁴<http://www.boost.org/doc/libs/release/libs/spirit/>

¹⁵<http://www.vtk.org>

¹⁶<http://www.paraview.org/>

¹⁷<https://wci.llnl.gov/simulation/computer-codes/visit>

We have also written a plugin for VisIt that reads in the default (`GADGET`) snapshot format. It should also be possible to use the eXtensible Data Model and Format (XDMF)¹⁸ and the XDMF plugins for VisIt and Paraview, an approach taken by e.g. `SWIFT`. However, the current version of `SHADOWFAX` does not write the necessary XDMF file, so that it needs to be manually created.

5. Basic tests

To validate the code, we have used it to evaluate a number of test problems. These have been gathered into a `testsuite`, together with the necessary files to create the initial conditions, run the simulations, and analyze the results. Where possible, we have provided analytic solutions to compare with.

These tests are meant to be run as a general code check after every significant change in the code, and for this reason use relatively low resolution grids. We therefore will not focus on obtaining the best possible accuracy. Rather, we will focus on accuracy when we compare `SHADOWFAX` with other publicly available codes in a later section.

In this section, we describe the physical test problems currently in the `testsuite` and discuss their results. We do not describe tests that are used to verify the proper working of the program itself, like the `restarttest`, which checks if the program correctly restarts from restart files.

5.1. Spherical overdensity test

This test problem consists of a uniform box with unit length, in which a fluid with density 0.125 and pressure 0.1 is in rest. In the center of the box, a spherical overdense region with density 1, pressure 1, and radius 0.25 is inserted. This test corresponds to one of the Riemann solver tests in Toro (2009), but generalized to 2 or 3 dimensions to test geometrical aspects of the code as well.

The solution of this problem consists of an inward travelling rarefaction wave, a central contact discontinuity, and an outward travelling shock wave. The simulation results in 2 and 3 dimensions at time $t = 0.1$ are shown in Figure 5, together with a high resolution result for the equivalent 1D problem obtained using a finite volume method on a fixed 1D grid. The different features of the solution are clearly resolved.

5.2. Gresho vortex

For this test, a vortex in hydrostatic equilibrium is evolved for some time to check the local conservation of angular momentum. Inside a box with unit length and constant density 1, a 2D azimuthal velocity profile of the form (Springel, 2010)

$$v_\phi(r) = \begin{cases} 5r & 0 \leq r < 0.2 \\ 2 - 5r & 0.2 \leq r < 0.4 \\ 0 & 0.4 \leq r \end{cases} \quad (12)$$

¹⁸<http://www.xdmf.org>

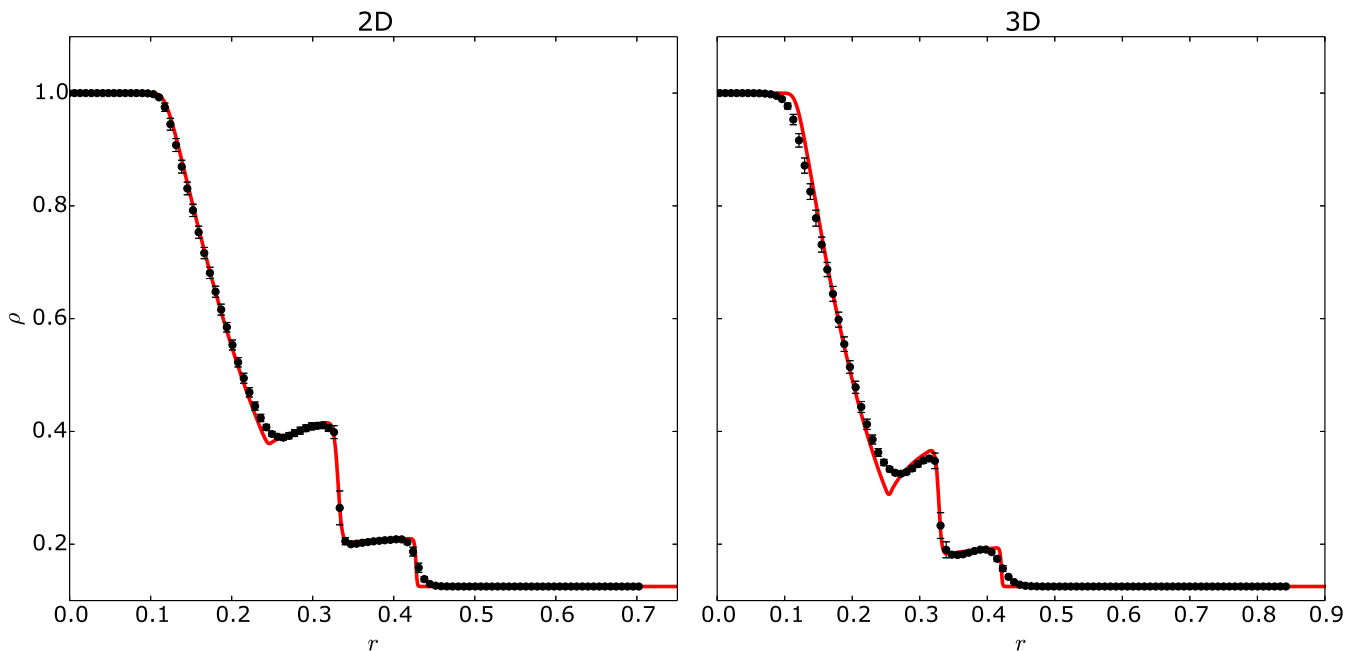


Figure 5: Radial density profile for the spherical overdensity test at time $t = 0.1$. *Left*: 2D result, using 10,000 uniformly sampled cells. *Right*: 3D result, using 100,000 uniformly sampled cells. The black dots are the simulation results, the red line corresponds to the solution of the high resolution 1D equivalent problem. To limit the number of data points, the simulation results have been binned, the standard deviation of the density within the bins is indicated by the error flags.

is balanced by a pressure profile of the form

$$p(r) = \begin{cases} 5 + \frac{25}{2}r^2 & 0 \leq r < 0.2 \\ 9 + \frac{25}{2}r^2 - 20r + 4 \log\left(\frac{r}{0.2}\right) & 0.2 \leq r < 0.4 \\ 3 + 4 \log(2) & 0.4 \leq r. \end{cases} \quad (13)$$

In 3D, we use the same profile and expand it to cylinders in the third dimension, in a box of size $1 \times 1 \times 1/3$. We evolve the setup to time $t = 3$, and compare the velocity and pressure profile with the initial profiles. The results are shown in Figure 6.

Both the 2D and 3D test conserve the hydrostatic equilibrium relatively well over a long time scale. This means local angular momentum is conserved to a reasonable degree.

5.3. Sedov-Taylor blast wave

This problem is meant to test the limits of the code, both of the Riemann solver, the mesh regularization algorithm, and the time step criterion. It consists of a box with unit length in which a cold medium with density 1 and pressure 10^{-6} is in rest. In the central cell, we set the pressure to a much higher value, which corresponds to an energy input of 1, so that a strong explosion is initiated. To accurately capture the explosion, it is important that

- the central cells are kept regular at the start of the simulation

- the cells surrounding the center are given small enough individual time steps to be active when the shock arrives
- the Riemann solver is able to handle vacuum generating conditions to correctly estimate fluxes around the central cell

The resulting shock profile is self-similar and has an analytic solution (Sedov, 1977), which is shown together with the simulation results in Figure 7. Again, the simulation results are in line with the analytic solution, and the shock is well-resolved.

5.4. N-body test

This test is used to validate the gravitational part of the code, and uses cold dark matter instead of gas. Since gravity is not guaranteed to work in 2D, this problem is only provided in 3D.

A Plummer sphere (Plummer, 1911) with mass 1000 and scale parameter 1 is initiated inside a large box (the actual box is irrelevant for this specific problem, but SHADOWFAX always requires a simulation box to be present). The velocities of the particles are chosen so that the entire problem is independent of time. For convenience, we set the gravitational constant $G = 1$ for this problem. We adopt a gravitational softening length of 0.03.

In Figure 8, we show the initial density profile, and the density profile at time 1, when the system has evolved for ~ 10 dynamical times. Figure 9 shows the relative error

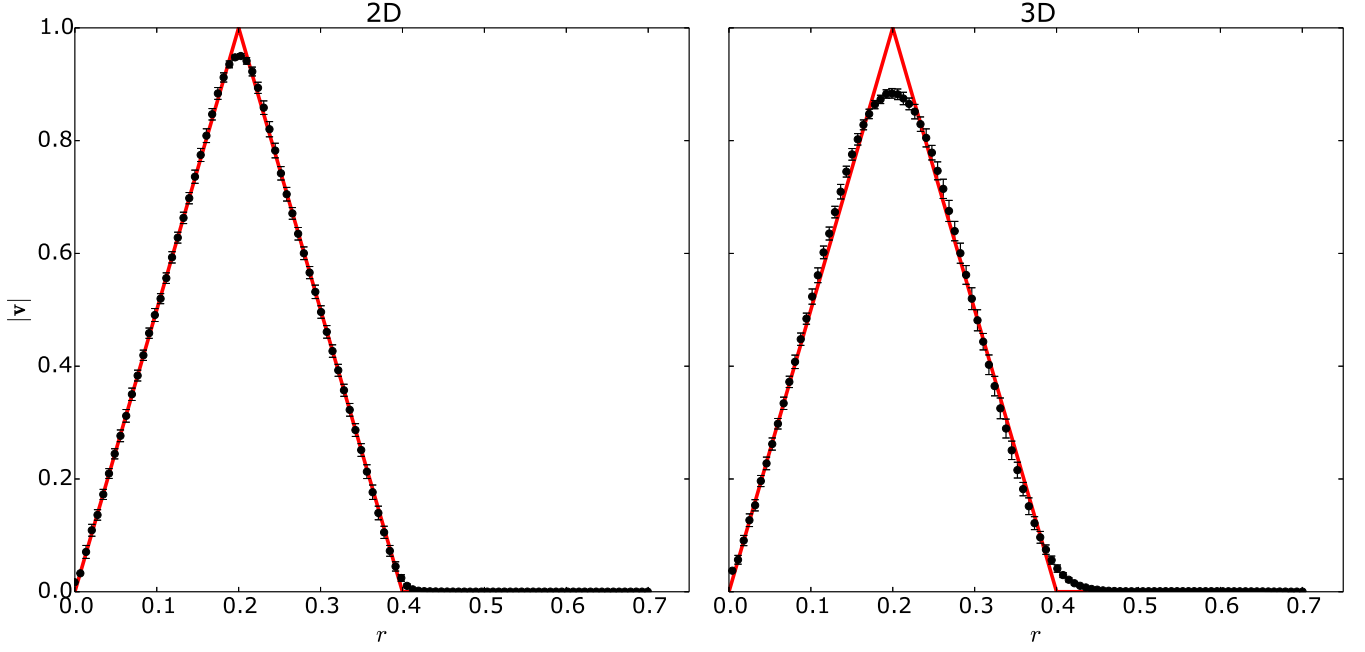


Figure 6: Radial velocity profile for the Gresho vortex test at time $t = 3$. Both the 2D and the 3D simulation use 10,000 uniformly sampled cells. The black dots represent the binned simulation results, with the error flags indicating the standard deviation on the values within the bins. The red line represents the initial velocity profile, which should remain constant.

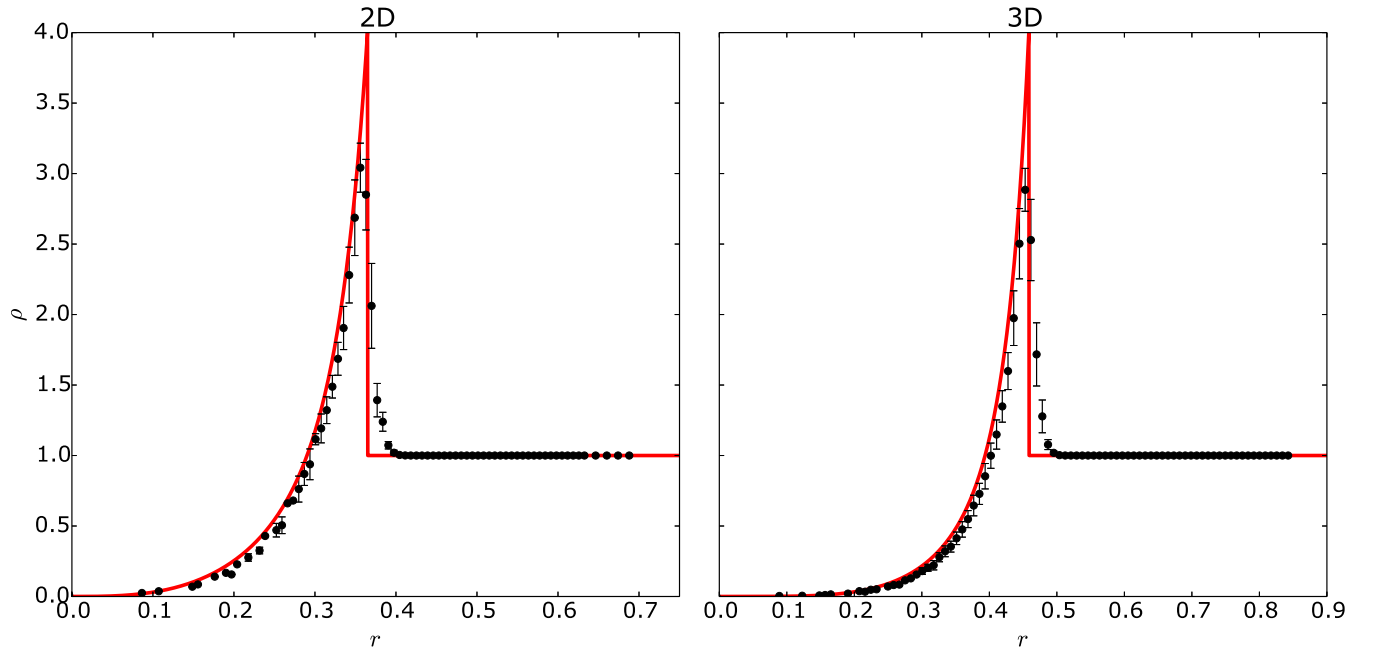


Figure 7: Density profile for the Sedov-Taylor blast wave test at time $t = 0.1$. Left: 2D version, using an initially Cartesian grid with 45×45 cells. Right: 3D version, using an initially Cartesian grid with $45 \times 45 \times 45$ cells. The black dots represent the binned simulation results, with the error flags indicating the standard deviation of the density values within the bins. The full red line is the analytical solution of Sedov (1977).

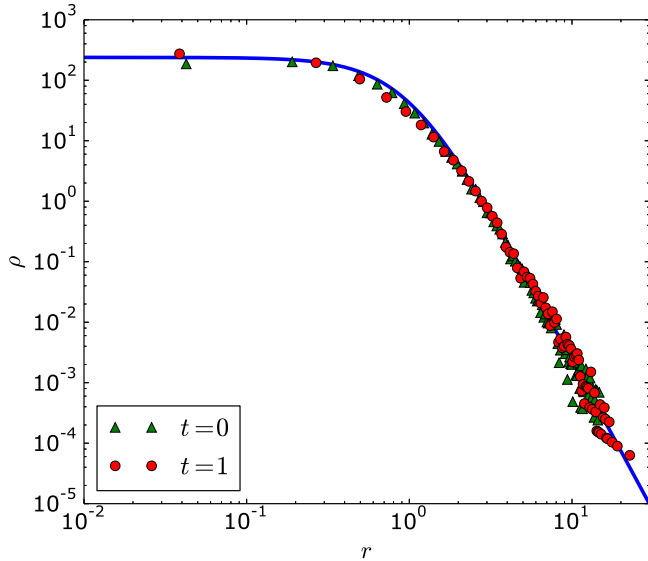


Figure 8: Density profile of the N-body test at the start and end of a simulation using 10,648 cold dark matter particles. The density is calculated by summing the masses of all particles within spherical shells. The dots and triangles represent simulation results, the full blue line is the theoretical Plummer density profile from which the initial condition is sampled.

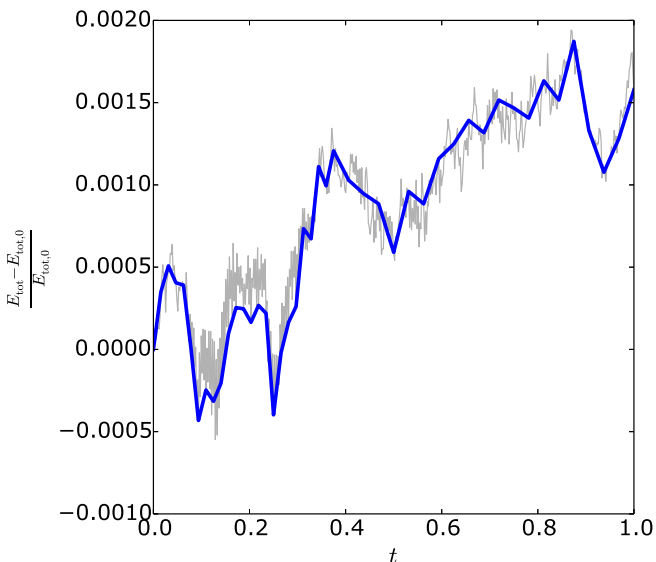


Figure 9: The relative energy error of the N-body test as a function of time. The gray line shows the energy error at all times, the blue line shows the energy error at the times when all particles are active.

on the total energy. We see that the system remains stable and that the total energy is quite accurately preserved.

5.5. Evrard collapse

This problem tests the coupling between hydrodynamics and gravity, and consists of a self-gravitating gas cloud with mass 1 and radius 1, with a density profile of the form (Springel, 2010)

$$\rho(r) = \begin{cases} \frac{1}{2\pi(r+0.001)} & r \leq 1 \\ 0 & 1 < r. \end{cases} \quad (14)$$

The cloud is initially at rest and has a very low pressure profile of the form

$$p(r) = \begin{cases} \frac{0.05}{3\pi(r+0.001)} & r \leq 1 \\ 0 & 1 < r, \end{cases} \quad (15)$$

corresponding to a low constant thermal energy. We set the gravitational constant $G = 1$ for this test and only consider a 3D version. The softening length is set to 0.003.

The vacuum boundary of the cloud poses a challenge for our finite volume method, since small numerical errors on the fluxes might easily cause non-physical negative masses and energies in the empty cells that surround the cloud. It forms a good test for our flux limiter and the overall stability of the code, while at the same time not contributing significantly to the result.

The density, radial velocity and entropy profiles of the simulation at time $t = 0.81$ are shown in Figure 10, together with a high resolution result for the equivalent 1D problem obtained using a finite volume method on a fixed 1D grid, and the solution of the same setup using the SPH code GADGET2. The relative error on the total energy is shown in Figure 11. The virializing shock is clearly resolved and travels at the expected speed. We see that total energy fluctuates when the shock is formed and stabilizes after the system has virialized, which indicates that the gravitational correction terms in our scheme are not entirely effective at the current resolution. Better energy conservation can be obtained by using more resolution, but this is too computationally expensive for the testsuite.

6. Convergence rate

The MUSCL-Hancock finite volume method implemented in SHADOWFAX is nominally second order in both space and time. However, due to the use of slope limiters and flux limiters, the actual order of the method can be lower in the presence of strong discontinuities. To test this, we study the convergence rate as a function of the number of cells for a number of different tests: a one dimensional smooth travelling sound wave, a one dimensional shock tube and a two dimensional vortex.

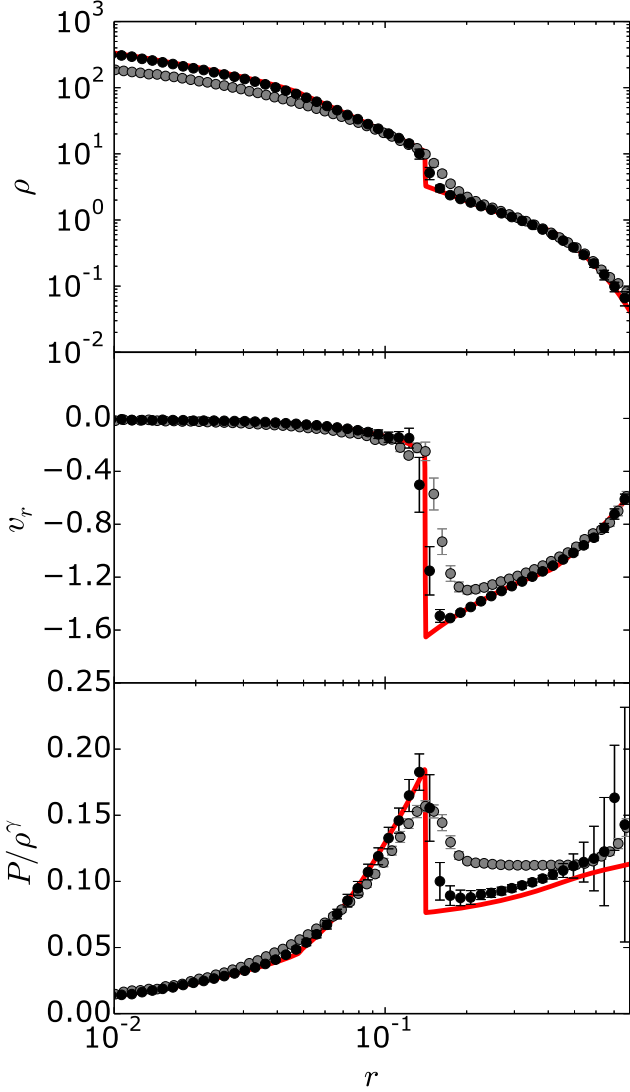


Figure 10: Profiles of the Evrard collapse test at time $t = 0.81$, when the central virializing shock has formed, but has not yet reached the boundary of the cloud. Top: density profile, middle: radial velocity profile, bottom: entropy profile. The simulation used 20,000 cells in total, some of which are vacuum cells surrounding the cloud. The black dots represent the binned simulation results, with error bars indicating the standard deviation on the density values within the bins. The red line is the solution of the equivalent 1D problem. The gray points are the solution for the same setup, but using the SPH code GADGET2.

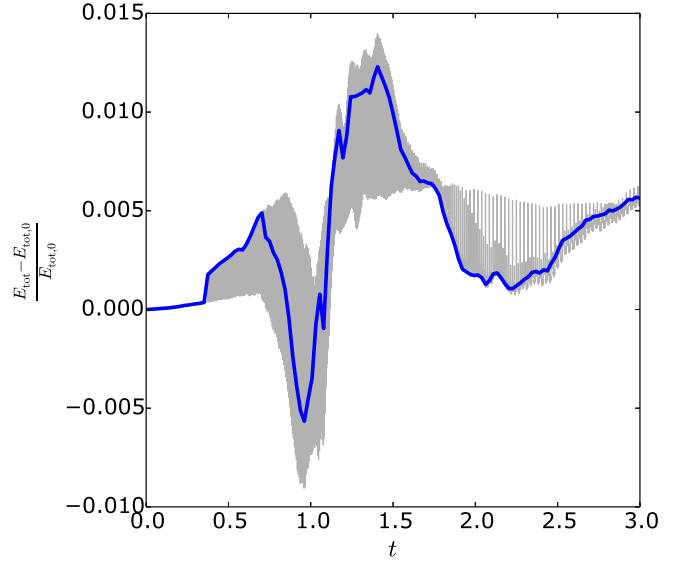


Figure 11: The relative energy error for the Evrard collapse test as a function of time. The gray line represents the energy error at all times, the blue line represents the energy error at times when all cells are active.

6.1. Sound wave

The initial condition for this test consists of a periodic cubic box with unit side containing a sound wave with a small amplitude $A = 10^{-6}$. The density is given by

$$\rho(x) = 1 + A \sin 2\pi x, \quad (16)$$

the pressure is $p(x) = \rho(x)^\gamma / \gamma$, with $\gamma = 5/3$, and the velocity is zero everywhere. The wave travels with the sound speed, $c_s = 1$ for this particular choice of pressure.

Although this problem is formally one dimensional, we study it in 3D, using N^3 comoving cells, with N the number of cells in one dimension. We use both an initial Cartesian grid (which remains Cartesian throughout the simulation as the fluid velocity is zero), and a random uniform grid. We expect the convergence to be better in the former case, as the Cartesian solution corresponds to a combination of N^2 1D solutions. For a random uniform grid, the cells are irregularly shaped, and the problem is effectively multi-dimensional.

We study the convergence rate by comparing the solution ρ_i at $t = 1$, when the wave has travelled for one box length, with the initial condition $\rho(x_i)$ at $t = 0$. To this end, we calculate the L1 norm

$$\text{L1} = \frac{1}{N^3} \sum_i |\rho_i - \rho(x_i)|, \quad (17)$$

for all cells i .

Figure 12 shows the L1 norm as a function of the equivalent 1D cell number N . Both the Cartesian and the random uniform grid show close to N^{-2} scaling, indicating that the method is indeed second order in space and time.

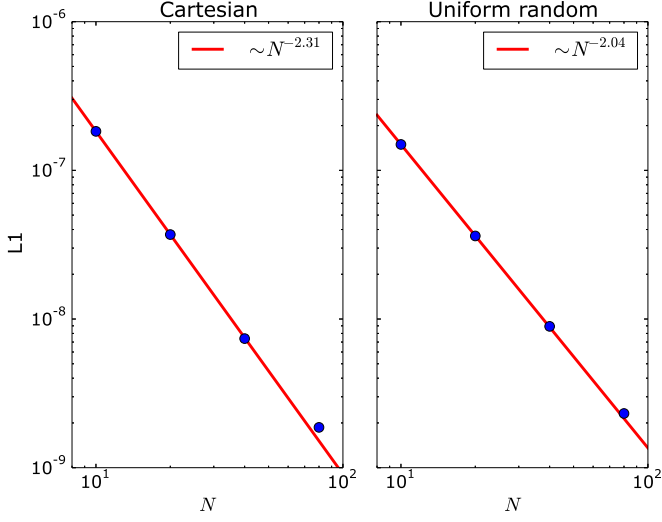


Figure 12: L1 norm as a function of 1D cell number for a travelling sound wave in 3D. The blue dots are the simulation results, the red line is a least squares fit.

6.2. Sod shock

A more demanding test problem is the Sod shock test, which consists of a reflective cubic box with unit length in which the density is given by

$$\rho(x) = \begin{cases} 1 & x < 0.5 \\ 0.25 & 0.5 \leq x, \end{cases} \quad (18)$$

and the pressure by

$$\rho(x) = \begin{cases} 1 & x < 0.5 \\ 0.1795 & 0.5 \leq x. \end{cases} \quad (19)$$

The initial velocity is zero everywhere. This problem is the 1D equivalent of the spherical overdensity discussed as part of the testsuite, and its solution has the same characteristic wave components, including a contact discontinuity and a shock wave, for which we expect the convergence rate of our scheme to be worse than second order.

We evolve the test to $t = 0.12$, and calculate the L1 norm in the same way as above, but with $\rho(x_i)$ now given by the exact solution to the equivalent Riemann problem at $t = 0.12$, which can be found using an exact Riemann solver.

Figure 13 shows the L1 norm as a function of the equivalent 1D cell number N , again for both a Cartesian initial grid and a random uniform initial grid. In this case, convergence is clearly worse than N^{-2} , and is not even first order in space and time. There no longer is a clear difference between the Cartesian grid and the uniform random grid.

6.3. Gresho vortex

To study the convergence in a manifestly multi-dimensional problem, we also consider the 2D Gresho vortex, which

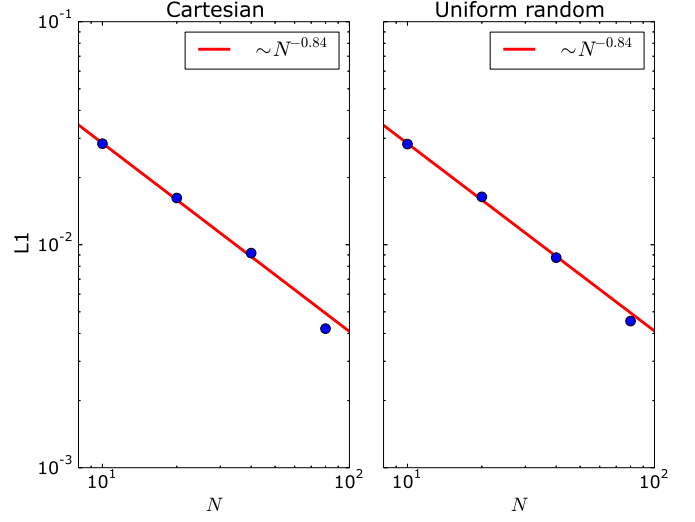


Figure 13: L1 norm as a function of 1D cell number for a Sod shock test in 3D. The blue dots are the simulation results, the red line is a least squares fit.

we already encountered as part of the testsuite. We run four simulations with respectively 1,000, 10,000, 50,000 and 100,000 random uniform cells until $t = 3$, and calculate the L1 norm for the azimuthal velocities $v_{\phi,i}$ using the time independent initial condition $v_{\phi}(r)$ given above:

$$L1 = \frac{1}{N} \sum_i |v_{\phi,i} - v_{\phi}(r_i)|. \quad (20)$$

In Figure 14, we show the L1 norm as a function of the 1D equivalent cell number $N' = \sqrt{N}$. Again, convergence is not second order, but it is clearly better than in the case of a strong shock, as the Gresho vortex is overall more smooth.

7. Performance

Modern high performance computing systems consist of large numbers of computing nodes, each of which can have multiple CPUs, which are made up of multiple computing cores. These systems are hence highly parallel and employing their full power requires algorithms that can exploit this parallelism. Compared to the available computing power, memory is relatively scarce on most system, so that it is also important to minimize the memory imprint of an application.

The current version of SHADOWFAX was not optimized for usage on high performance systems, but some basic MPI communication instructions were added to make it run on distributed memory systems. To fully exploit the power of modern architectures, a hybrid algorithm that combines distributed memory parallelism with shared memory parallelism is needed, as well as a better representation

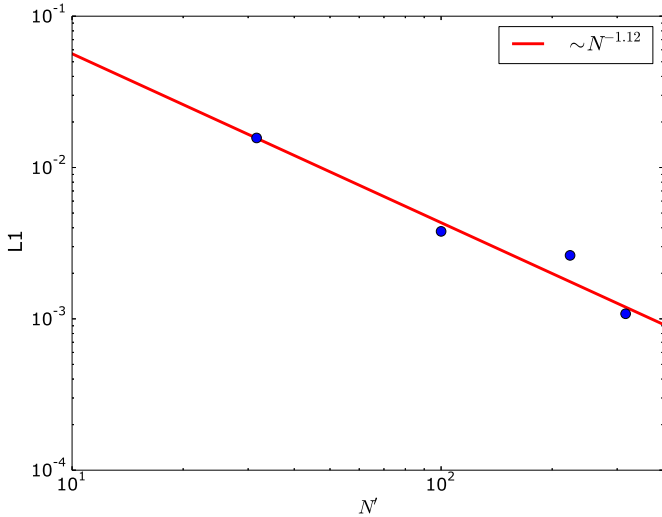


Figure 14: L1 norm as a function of 1D cell number for a 2D Gresho vortex test. The blue dots represent simulation values, the red line is a least squares fit.

of the Voronoi mesh that depends less on a globally constructed mesh. This requires a thorough refactoring of the code, which is left for future versions.

In this section, we discuss the strong and weak scaling of the current version of the code, the contribution of the various components of the code to the total run time, and their memory imprint. For all these tests, we use the Evrard collapse test discussed above, which uses both the hydrodynamical solver and the N-body solver. Since this setup is very inhomogeneous, our simple domain decomposition leads to serious load-imbalances. For comparison, we also show scaling results for the more homogeneous spherical overdensity test.

7.1. Strong scaling

Strong scaling measures the decrease in total simulation run time when running the same simulation on an increasingly large number of processes. Ideally, doubling the amount of processes should half the total run time, but due to communication overhead this can never be achieved. As communication scales with the surface area of the different computational domains in the simulation, while the computation time per domain scales with the domain volume, we expect the relative contribution of communication to the total run time to increase with increasing process number. This poses a natural limit on the speed up that can be achieved for a given problem size.

Figure 15 shows the strong scaling for two of the test problems that are part of the testsuite: the 3D Evrard collapse and the 3D spherical overdensity. The tests were run on a single node of our local computing cluster, consisting of 4 2.7 GHz Intel Xeon CPUs with 8 cores each, using version 4.8.4 of the GNU compiler and OpenMPI 1.6.5. The top row shows the speedup, i.e. the ratio of the single

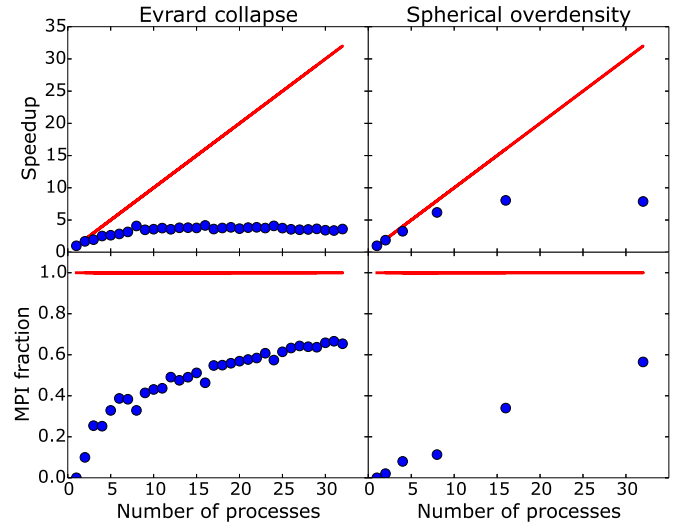


Figure 15: Speedup and MPI fraction for two different tests from the testsuite under strong scaling.

process total run time and the parallel run time. The bottom row shows the fraction of the total run time spent in MPI functions: send and receive operations and idle time due to load imbalances. We see that the speedup is rather poor, except for small process numbers, and that the MPI fraction increases significantly with increasing number of processes. This is to be expected, since load balancing is in no way optimized in the current version of the code. For a homogeneous set up like the spherical overdensity this leads to reasonable scaling, but for strongly inhomogeneous tests like the Evrard collapse this is disastrous.

7.2. Weak scaling

Weak scaling is the scaling behaviour of the code when increasing the number of processes for a fixed problem size per process, i.e. if we double the number of processes, we double the number of cells in the simulation as well. It is a good measure for how well the problem is split up over the different processes, as we expect the amount of work and the amount of communication per process to stay roughly constant.

Figure 16 shows the weak scaling for the 3D Evrard collapse and 3D spherical overdensity, with a nominal load of 10,000 cells per process for both tests. The tests were carried out on the same hardware as the strong scaling tests discussed above. Instead of the speedup, we now show the slowdown in the top row, i.e. the ratio of the total parallel run time and the serial run time. Again, we have rather poor scaling.

7.3. Components

An important part of a SHADOWFAX simulation is the construction of the Voronoi mesh that is used for the hydrodynamical integration. On average, the serial version of our code can handle $\approx 90,000$ Voronoi cells per second

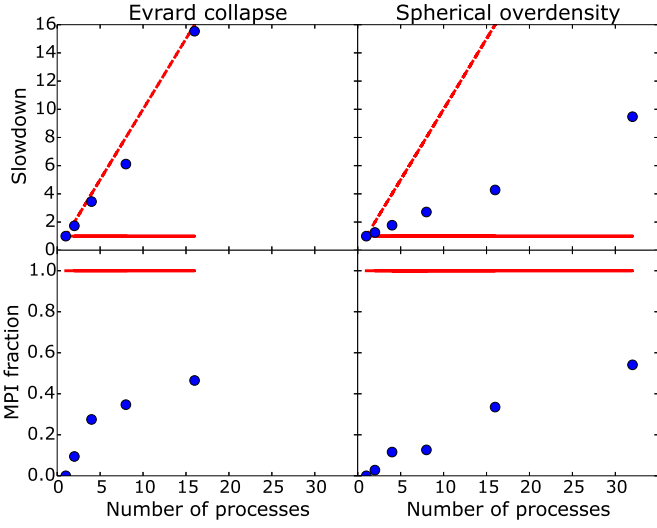


Figure 16: Slowdown and MPI fraction for two different tests from the testsuite under weak scaling. The red dashed line corresponds to a 1:1 relation, while the full red lines correspond to unity.

in 2D, and $\approx 15,000$ Voronoi cells per second in 3D, including the treatment of reflective or periodic boundaries and the calculation of cell centroids and volumes, and face midpoints and surface areas.

Figure 17 shows the amount of time spent in various parts of the code during serial runs with different problem sizes. The current design of the code makes it very hard to extract the time spent in MPI communications from the times for the different components, so that we do not show parallel results.

The gravitational force calculation clearly makes up a large fraction of the total run time, which increases if the number of cells is increased. Grid construction in 3D takes up about double the time that is spent in the actual hydrodynamical integration. Only very little time is spent in other parts of the algorithm, e.g. particle sorting, tree construction, snapshot output... Program performance hence does not suffer due to the somewhat less efficient but much more convenient object oriented design of these parts.

7.4. Memory consumption

To test the memory consumption of the code, we used MASSIF¹⁹, a heap profiler which is part of the VALGRIND instrumentation framework²⁰. Since we do not expect the memory imprint to vary much over time, we limited the Evrard test to $t = 0.06$ for this test.

Figure 18 shows the fraction of the memory occupied by various parts of the code during the final MASSIF snapshot, when the code used 137 MB of memory in total (including empty blocks used for memory alignment). A large fraction of this memory is occupied by the Voronoi mesh,

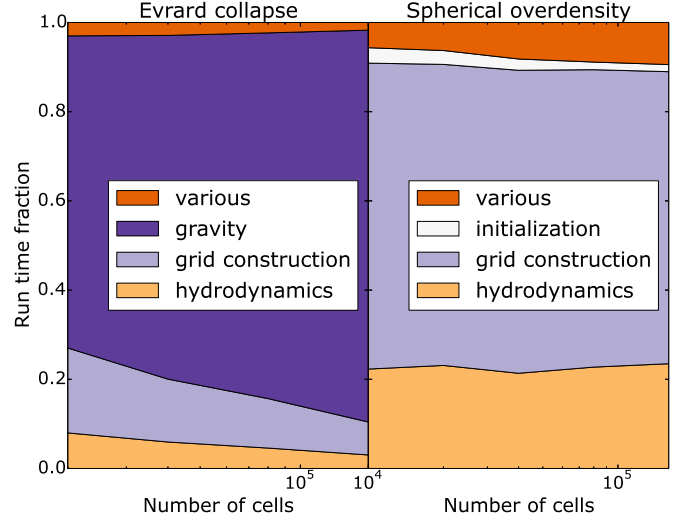


Figure 17: Fraction of total run time spent in different parts of the code.

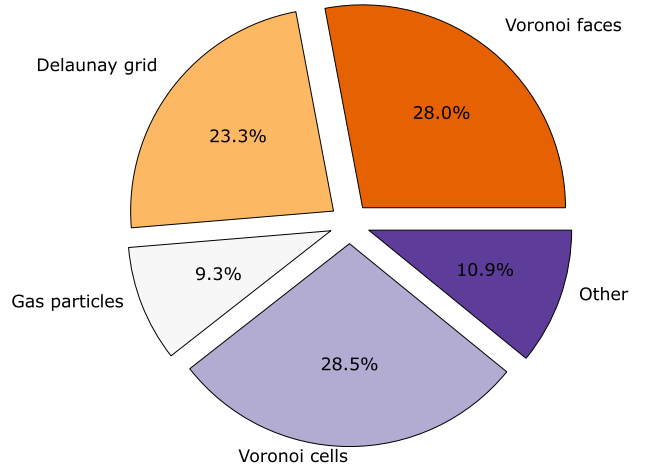


Figure 18: The fraction of the memory occupied by various parts of the code during an Evrard collapse test with 20,000 cells.

¹⁹<http://valgrind.org/docs/manual/ms-manual.html>

²⁰<http://valgrind.org/>

with only a small fraction of the memory used to store the particle properties and the tree structure needed for the gravity calculation. Note that both the Delaunay tessellation and the Voronoi mesh are stored simultaneously in the current version, while the Delaunay tessellation can actually be discarded after the Voronoi mesh has been constructed. This is left as a future optimization.

8. Comparison with other methods

In this section, we compare SHADOWFAX with a number of other publicly available hydrodynamical solvers, to qualify the advantages and disadvantages of the moving mesh method. All files necessary to run these tests are available from <http://www.dwarfs.ugent.be/shadowfax/>.

8.1. Kelvin-Helmholtz instabilities

It is a known problem of particle-based Lagrangian methods like SPH that they have difficulties resolving Kelvin-Helmholtz instabilities (Agertz et al., 2007), since the basic SPH equations do not cover discontinuous solutions, like shock waves and contact discontinuities. As Springel (2010) showed, a moving mesh method does not experience these difficulties, as the Riemann problem based finite volume method that is used does include discontinuous solutions.

One of the main advantages of a Lagrangian method over methods that use a fixed discretization (like AMR), is the Galilean invariance of the method. This means that the flux between two neighbouring cells will only depend on the relative velocity of two neighbouring cells, and not on their absolute velocities with respect to some reference frame fixed to the simulation box. As a result, we expect a moving mesh method to better resolve instabilities in a fluid that is moving with a high bulk velocity with respect to the simulation box reference frame. To quantify this behaviour, we set up a variant of the shearing layers test introduced in Agertz et al. (2007).

For this test, two layers which can have different densities are in pressure equilibrium inside a periodic box. The layers receive a velocity component parallel to the interface between the layers, but with opposite sign, so that they shear against each other. Due to the pressure equilibrium, the system is marginally stable : a small velocity component perpendicular to the interface between the layers will exponentially grow to form a Kelvin-Helmholtz instability. The instability first goes through a linear phase of exponential growth, after which the system becomes highly non-linear. The simple setup described here is unstable on all scales, so that instabilities can even be seeded by numerical noise in the absence of diffusion. As a result, the results are highly dependent of the resolution and the details of the numerical scheme. This makes a thorough comparison of different methods completely impossible (Lecoanet et al., 2016).

As Hendrix and Keppens (2014) point out, introducing a middle layer with a linear transition in flow velocity

in between the shearing layers will suppress small scale instabilities, so that the growth of instabilities no longer depends on the numerical resolution (if it is high enough). The middle layer also introduces a maximally unstable wavelength, which we will seed. This gives us full control over the instabilities that will grow. We first discuss the non-linear growth of the instability in a setup with a density contrast of 10 between the layers, to show that SHADOWFAX qualitatively produces similar instabilities. We then study the convergence of the linear growth rate in a setup without density contrast.

8.1.1. Bulk velocity

We set up a periodic 2D box with unit length, in which the density is given by

$$\rho(x, y) = \begin{cases} 1 & y < 0.25 \\ 10 & 0.25 \leq y \leq 0.75 \\ 1 & 0.75 < y. \end{cases} \quad (21)$$

The x component of the velocity is given by

$$v_x = \begin{cases} -0.5 & y \leq 0.25 - d \\ -0.5 + \frac{y+d-0.25}{2d} & 0.25 - d < y < 0.25 + d \\ 0.5 & 0.25 + d \leq y \leq 0.75 - d \\ 0.5 - \frac{y+d-0.75}{2d} & 0.75 - d < y < 0.75 + d \\ -0.5 & 0.75 + d \leq y, \end{cases} \quad (22)$$

with $d = 0.025$ the thickness of the middle layer. The y component of the velocity is

$$v_y = A \sin(4\pi x) \left(e^{-\frac{(y-0.25)^2}{2\sigma^2}} + e^{-\frac{(y-0.75)^2}{2\sigma^2}} \right), \quad (23)$$

with $A = 0.1$ and $\sigma = 0.00125$. The pressure in the entire box is set to the constant value $p = 2.5$.

We compare the results obtained with SHADOWFAX, with results obtained using the AMR code MPI-AMRVAC²¹ (Keppens et al., 2012), using the same initial condition (we use a Cartesian initial grid for the SHADOWFAX runs). MPI-AMRVAC supports different hydrodynamical schemes; we use both a conservative finite difference scheme with global Lax-Friedrich splitting and a fifth order spatial reconstruction (hereafter called FD), and a finite volume scheme with a Harten-Lax-van Leer Contact (HLLC) solver (hereafter called FV). Both schemes use a fourth order accurate Runge-Kutta time integration scheme.

To test the Galilean invariance of the code, we optionally add a bulk velocity $v_{\text{bulk}} = 100$ to the entire fluid (corresponding to a Mach number of 155 in the high density layer), so that the fluid moves with respect to the simulation box reference frame. The results of a low resolution run at time $t = 1.5$ are shown in Figure 19. Without a bulk velocity, the three methods produce similar

²¹ascl:1208.014

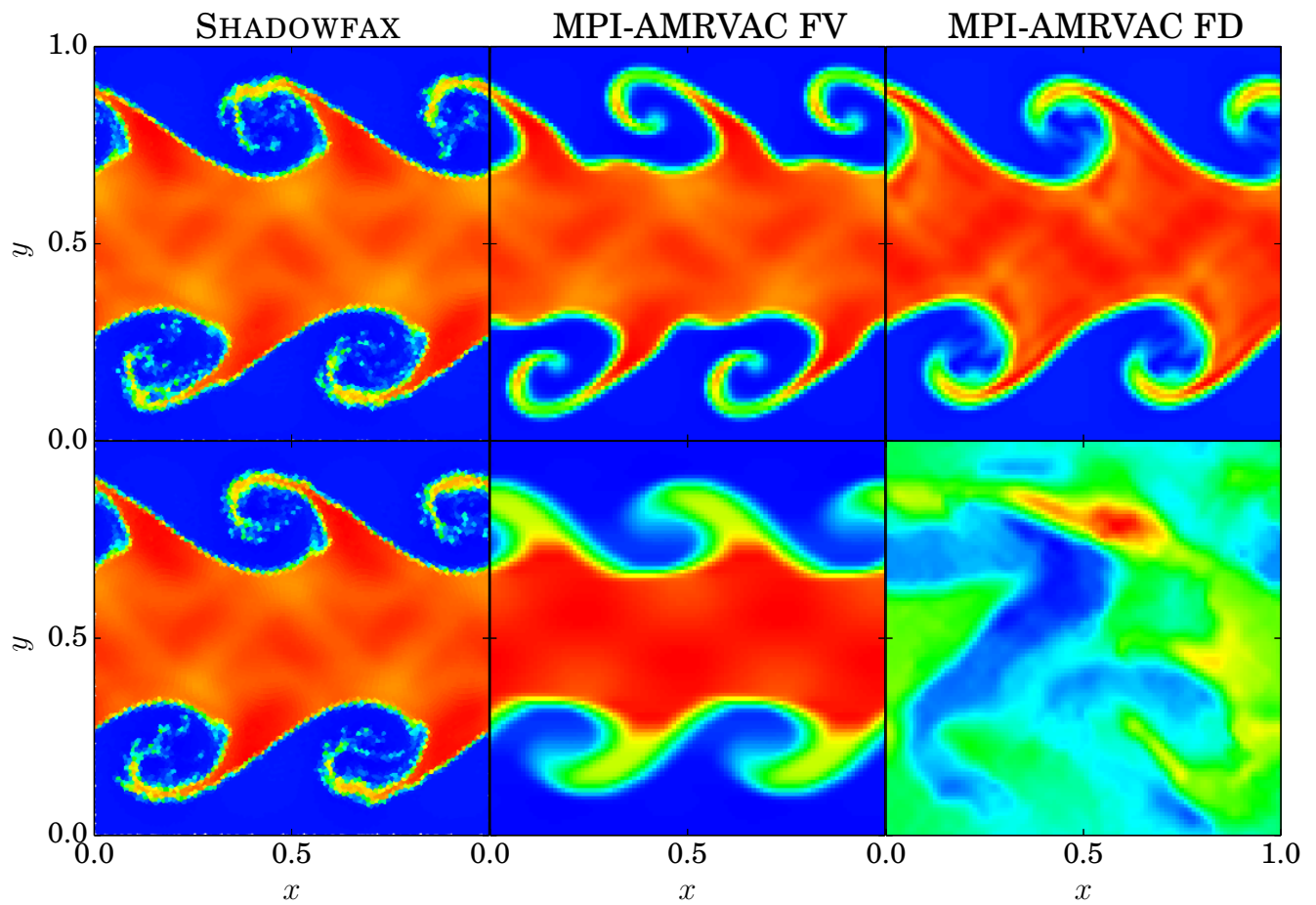


Figure 19: Density colour plot for the shearing layers test at time $t = 1.5$. The top row corresponds to simulations with $v_{\text{bulk}} = 0$, while the bottom row corresponds to simulations with $v_{\text{bulk}} = 100$. All simulations start from a 100×100 Cartesian grid and have a fixed number of cells. The individual cells are shown, this explains the irregularities at the boundaries of the SHADOWFAX plot.

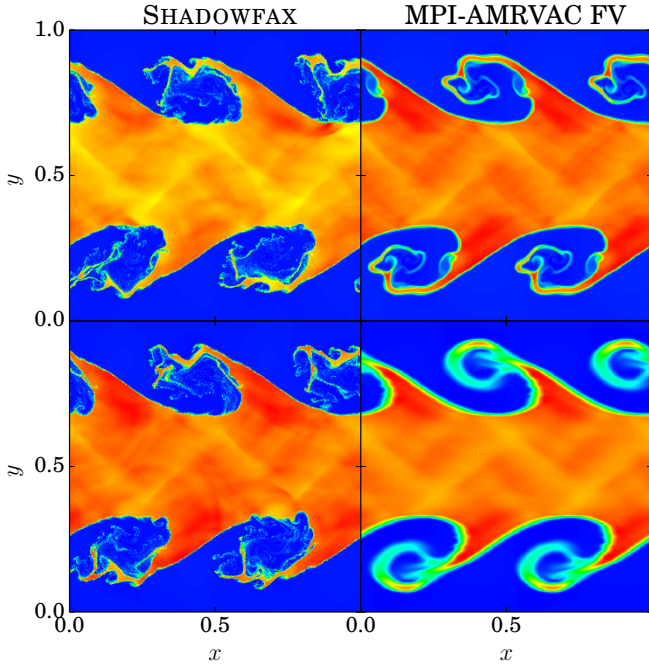


Figure 20: Density colour plot for the shearing layers test at time $t = 1.5$ for simulations using a 400×400 grid. The top row corresponds to simulations with no bulk velocity, the bottom row has $v_{\text{bulk}} = 100$.

results, in the sense that they all produce the same large instabilities on the same timescale. There are some differences in the non-linear phase of the instability, which is to be expected. With a bulk velocity, the results dramatically change for the MPI-AMRVAC simulations. The FD method does not produce any result at all, while the instabilities in the FV simulation are clearly affected by the bulk velocity. There is also a clear imprint on the run time of the MPI-AMRVAC simulations, since a much smaller system time step is needed for the integration. The run time and the results of the SHADOWFAX simulations are not affected by the bulk velocity, since the mesh is moving along with the flow. These results are confirmed by the high resolution runs, shown in Figure 20.

8.1.2. Linear growth rate

In a setup without density contrast, the initial exponential growth of the instability only depends on the wavelength of the instability and the thickness of the middle layer (Hendrix and Keppens, 2014). This means that simulations of this initial phase should converge to the same growth rate, irrespective of the resolution or the method that is used.

To test this, we run a variant of the shearing layers test without density contrast. We still use a periodic box with unit length, but now the density and pressure in the box are both constant and equal to 1. The x component of the velocity is given by (22), while the y component of

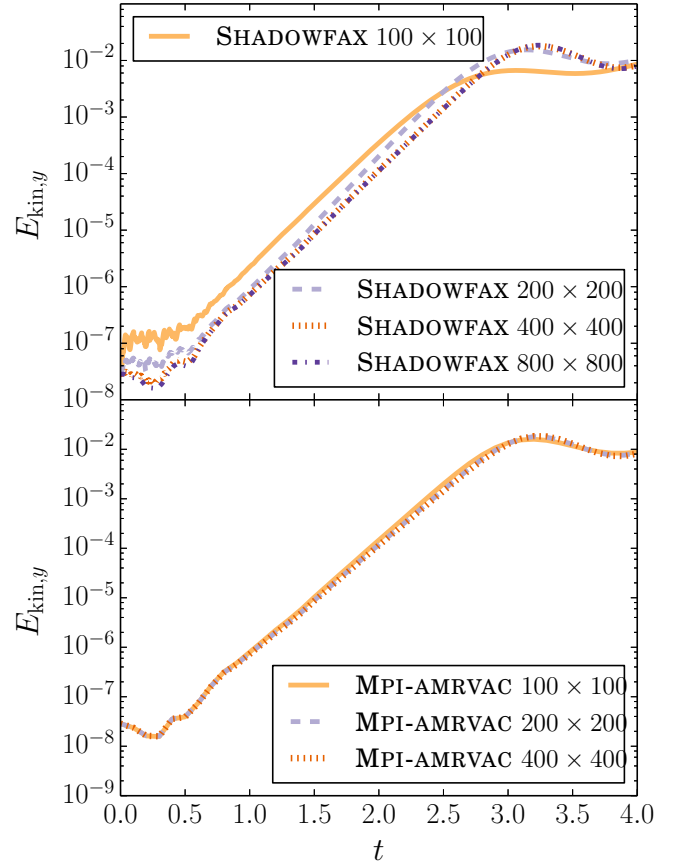


Figure 21: The kinetic energy in the y direction as a function of time for the shearing layers test without a density contrast.

the velocity is now given by

$$v_y = B \sin(4\pi x) \left(e^{-\frac{(y-0.25)^2}{32d^2}} + e^{-\frac{(y-0.75)^2}{32d^2}} \right), \quad (24)$$

with $B = 0.0005$ and $d = 0.0317$.

To quantify the growth of the instability, we track the total kinetic energy in the y direction. Initially, this energy is set by our seed velocity, but as the instability grows, kinetic energy in the x direction is converted into extra kinetic energy in the y direction, so that this energy will grow exponentially, as does the y component of the velocity.

Figure 21 shows the kinetic energy in the y direction as a function of time for our simulations and for grids with different resolutions. The high resolution SHADOWFAX results are in good agreement with the high resolution MPI-AMRVAC results, but the convergence is slower for SHADOWFAX. This is illustrated in Figure 22, where we plot the relative difference between the different simulations and the high resolution MPI-AMRVAC result, that we use as a reference solution.

We fitted an exponential function of the form Be^{At} to the kinetic energy in the y direction, in the time interval $[1.5, 2.5]$, and use the slope A to quantify the growth of the

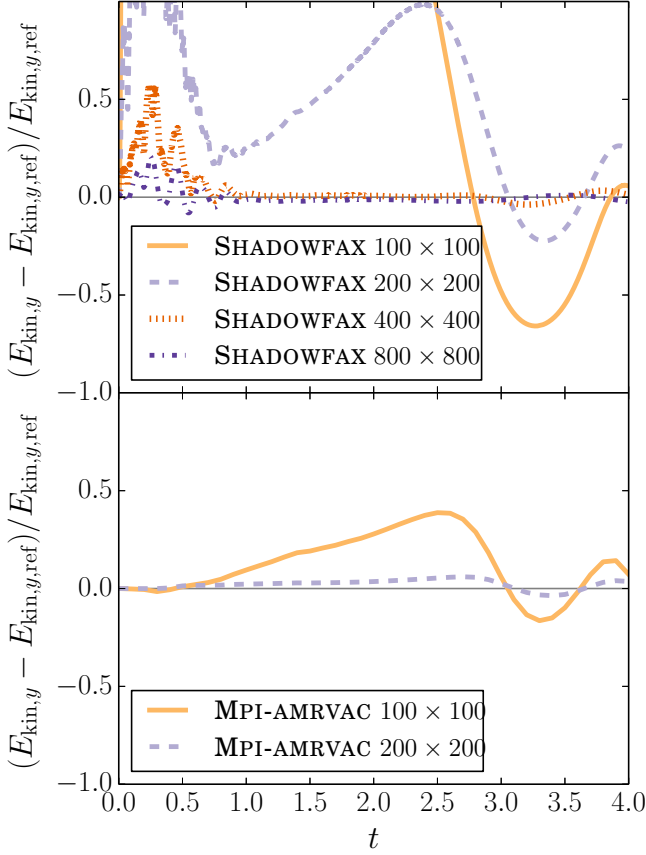


Figure 22: The relative difference between the kinetic energy in the y direction for the 400×400 MPI-AMRVAC simulation and that for the other simulations, as a function of time.

Table 1: Slope of an exponential fit to the kinetic energy in the y direction in the time interval $[1.5, 2.5]$ for the shearing layers tests without density contrast.

simulation	slope
SHADOWFAX 100×100	4.61
SHADOWFAX 200×200	5.43
SHADOWFAX 400×400	5.10
SHADOWFAX 800×800	5.10
MPI-AMRVAC 100×100	5.28
MPI-AMRVAC 200×200	5.14
MPI-AMRVAC 400×400	5.12

instability. The results are shown in Table 1. Both the high resolution SHADOWFAX and MPI-AMRVAC results are converged.

8.2. SHADOWFAX versus SWIFT

The mesh-free methods introduced by Hopkins (2015) use the same finite volume method used by SHADOWFAX, but use an SPH-like discretization of the fluid to calculate volumes and interfaces between neighbouring particles. Since this method does not require the construction of a global unstructured mesh, it is computationally cheaper and has a better potential for parallel scalability. Just as SPH however, the method smooths out local resolution over a number of neighbouring particles, potentially lowering the effective resolution.

We compare SHADOWFAX with our own implementation of a mesh-free method in the highly parallel SPH-code SWIFT²². This method combines the fast neighbour loop algorithms of SWIFT with a finite volume method that is the same as implemented in SHADOWFAX, and uses the same exact Riemann solver. Since SHADOWFAX reads the same initial condition file format as SWIFT, we can use the exact same initial condition for both simulations and directly compare the results. We also compare with the default SPH version of SWIFT.

Figure 23 shows the density profile of a Sod shock test, which is the 1D equivalent of the spherical overdensity test discussed as part of the `testsuite`. A left high density, high pressure region with $\rho = 1$ and $p = 1$ connects with a low density, low pressure region with $\rho = 0.25$ and $p = 0.1795$ at $x = 0.5$ inside a cuboid with dimensions $1 \times 0.125 \times 0.125$ with periodic boundaries. The results are evolved to time $t = 0.12$, when the left rarefaction wave, central discontinuity and right shock have developed.

The SHADOWFAX result clearly follows the theoretical curve, while both SWIFT results show minor deviations around the different features in the profile. The deviations are strongest for the SWIFT mesh-free results, although the noise on the SWIFT SPH result is higher. We calculated χ^2 values for all three simulations by summing the quadratic differences between the particle densities and the theoretical densities for all particles. This yielded $\chi^2 = 29.96$ for SHADOWFAX, $\chi^2 = 106.71$ for SWIFT mesh-free, and $\chi^2 = 123.54$ for SWIFT SPH. Not smoothing out the local resolution hence clearly leads to an overall higher accuracy of the moving mesh method.

8.3. Noh test

The strong shock test proposed by Noh (1987) is a very challenging test with a known analytical solution. It consists of a reflective box with unit length, in which a fluid with unit density and a negligible thermal energy of 1×10^{-5} is enclosed. The radial velocity of the fluid is set

²²<https://gitlab.cosma.dur.ac.uk/swift/swiftsim/tree/gizmo>

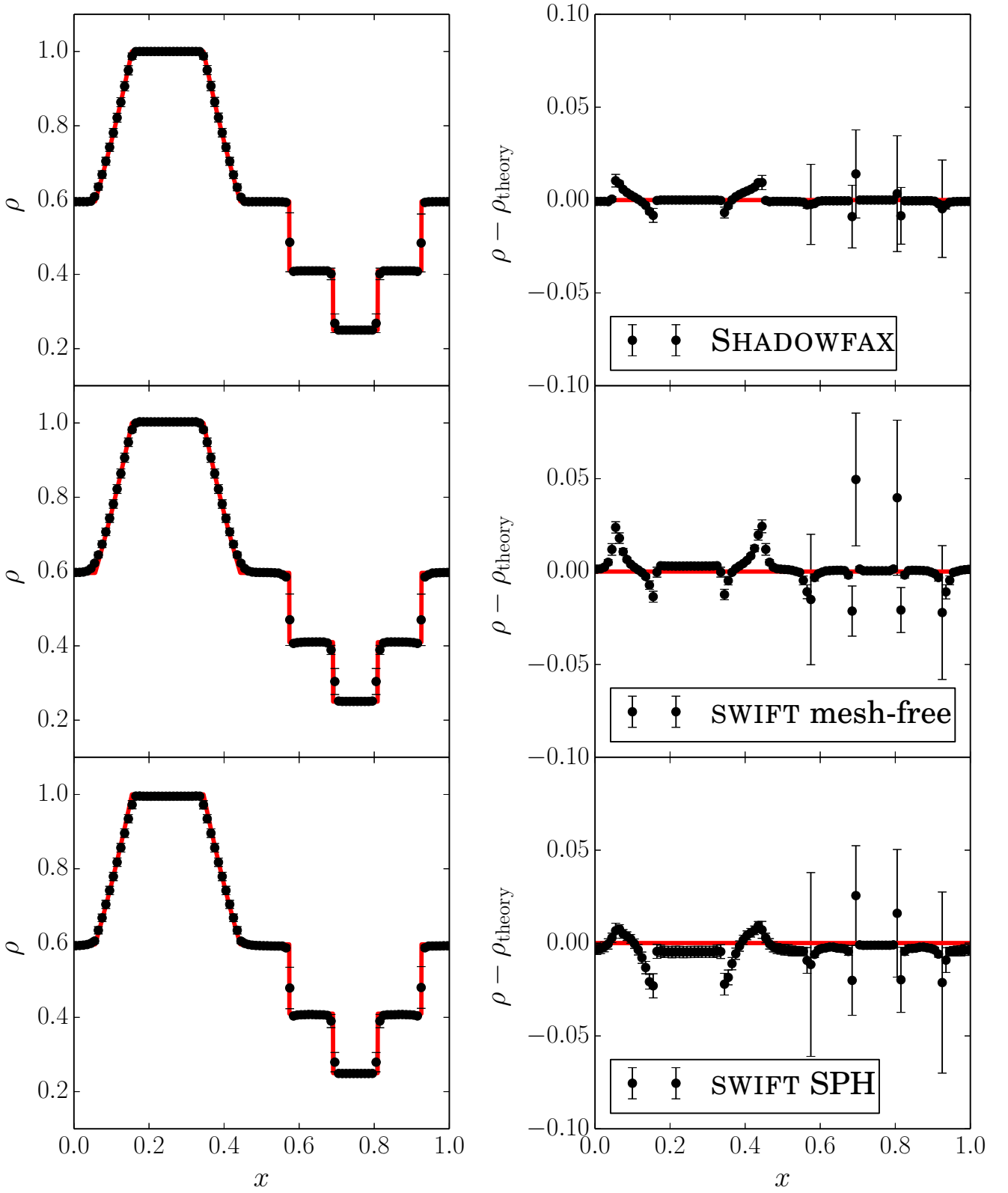


Figure 23: Density profile of the Sod shock test at $t = 0.12$. The black dots represent the binned density values, with the error flags indicating the standard deviation on the values within the bins. The red line corresponds to the exact solution, which is the solution of the equivalent Riemann problem. The right column shows the difference between the density and the analytical solution. All simulations use the same initial condition with 1,024,128 particles.

to -1 at $t = 0$, so that the fluid collapses on the origin and causes a strong shock with a very high Mach number.

The velocity of the shock front is $v_{\text{shock}} = 1/3$, and the radial density profile at time $t > 0$ is given by

$$\rho(r, t) = \begin{cases} 16 & r \leq v_{\text{shock}}t \\ 1 + \frac{t}{r} & v_{\text{shock}}t < r \end{cases} \quad (25)$$

in 2D.

As is common for this problem, we restrict ourselves to the upper right quadrant of the box. However, we do not use the commonly used inflow boundary conditions for the upper and right boundaries (Springel, 2010), since SHADOWFAX does not currently support inflow boundaries. Since the radial flow of the fluid creates a very low density cavity at these boundaries, this leads to numerical problems when the shock reaches the low density cavities. We will therefore restrict the simulation to $t = 0.5$ and use a higher resolution compared to Springel (2010), so that the lower left quarter of our box can be compared with his result. We only show the 2D version of the test. For comparison, we also run the same test using MPI-AMRVAC.

Figure 24 shows the radial density profile at $t = 0.5$, together with the analytical solution. The results for both methods are in good agreement, but the low resolution MPI-AMRVAC result has a density peak at the origin which is less pronounced in the SHADOWFAX result. We calculated χ^2 values for the simulations, yielding $\chi^2 = 1.78 \times 10^4$ and $\chi^2 = 1.55 \times 10^5$ for SHADOWFAX, and $\chi^2 = 2.87 \times 10^5$ and $\chi^2 = 4.54 \times 10^6$ for MPI-AMRVAC.

8.4. Implosion test

Another challenging test is the implosion test of Liska and Wendroff (2003). It consists of a periodic box of length 0.6×0.6 , in which a fluid with unit density and pressure is initially at rest. In the center of the box, a rhombus with width 0.3 is cut out, in which the density and pressure are given lower values: $\rho = 0.125$, $p = 0.14$. The high density fluid will implode into this region and cause a strong shock wave, that will travel back and forth in the periodic box. As in Liska and Wendroff (2003), we set the adiabatic index $\gamma = 1.4$ for this test.

This test involves both a large scale strong shock wave, and a lot of small scale instabilities at the interface between high and low density region, which interact with this shock wave. Since the initial conditions do not contain middle layers that could suppress small scale instabilities, the results in general will not converge. The behaviour of the strong shock wave is however similar for different methods, as Liska and Wendroff (2003) showed. It is furthermore interesting to see whether a code can handle this complex problem.

In Figure 25, we show some snapshots of the implosion test and compare SHADOWFAX results with results obtained using MPI-AMRVAC. It is interesting to see that both methods produce asymmetrical results in the center, while reproducing the same large scale shock wave, even

at later times, when the shock wave has interacted with the central instabilities. Just as before, the SHADOWFAX instabilities seem to develop faster than the ones in the MPI-AMRVAC result, and they are also significantly more chaotic, due to the co-moving character of the mesh. For the same mesh resolution, the SHADOWFAX results show more instabilities, indicating that a moving mesh has a higher local resolution. Figure 2 shows a zoom of the SHADOWFAX result at time $t = 0.5$ with the mesh overplotted, to illustrate how the mesh adapts to the local density.

We must however stress that the setup of this problem makes it impossible to compare these instabilities, and that it is impossible to determine if these instabilities are converged in any way. It is hence impossible to make a claim about which method is better. We can only point out the differences between both methods.

9. Discussion

In this paper, we introduced the public simulation code SHADOWFAX. The code can be used to simulate a mixture of gas and cold dark matter, with an accurate treatment of the hydrodynamics and gravitational forces. The discretization of the gas is provided by an unstructured Voronoi mesh, which is evolved in time to more accurately follow the hydrodynamical flow.

The code is inspired by Springel (2010), but uses an object-oriented design, which attempts to make the code easier to read and extend. Some parts of the code make use of advanced C++ language features, like templates, to improve code reuse without significant run time cost. We have attempted to separate the actual physics from the algorithmic details as much as possible. Much improvement is possible however, which will be the subject of future work on the code.

We have introduced the test problems that are currently included in the public version of the code, as well as some more involved tests that compare the code with other publicly available codes. These tests show that the Lagrangian nature of the moving mesh method makes it better at resolving instabilities in regions with high Mach numbers than fixed grid methods. On the other hand, a moving mesh is a lot more sensitive to instabilities that are seeded numerically. When the growth rate of instabilities is studied, a moving mesh method requires higher resolution to converge to a consistent growth rate than a fixed grid method.

The finite volume method used by SHADOWFAX is almost identical to that used by the mesh-free methods of Hopkins (2015), but has a higher effective resolution for the same number of particles, since the mesh-free discretization of space smooths out resolution over a large number of neighbours.

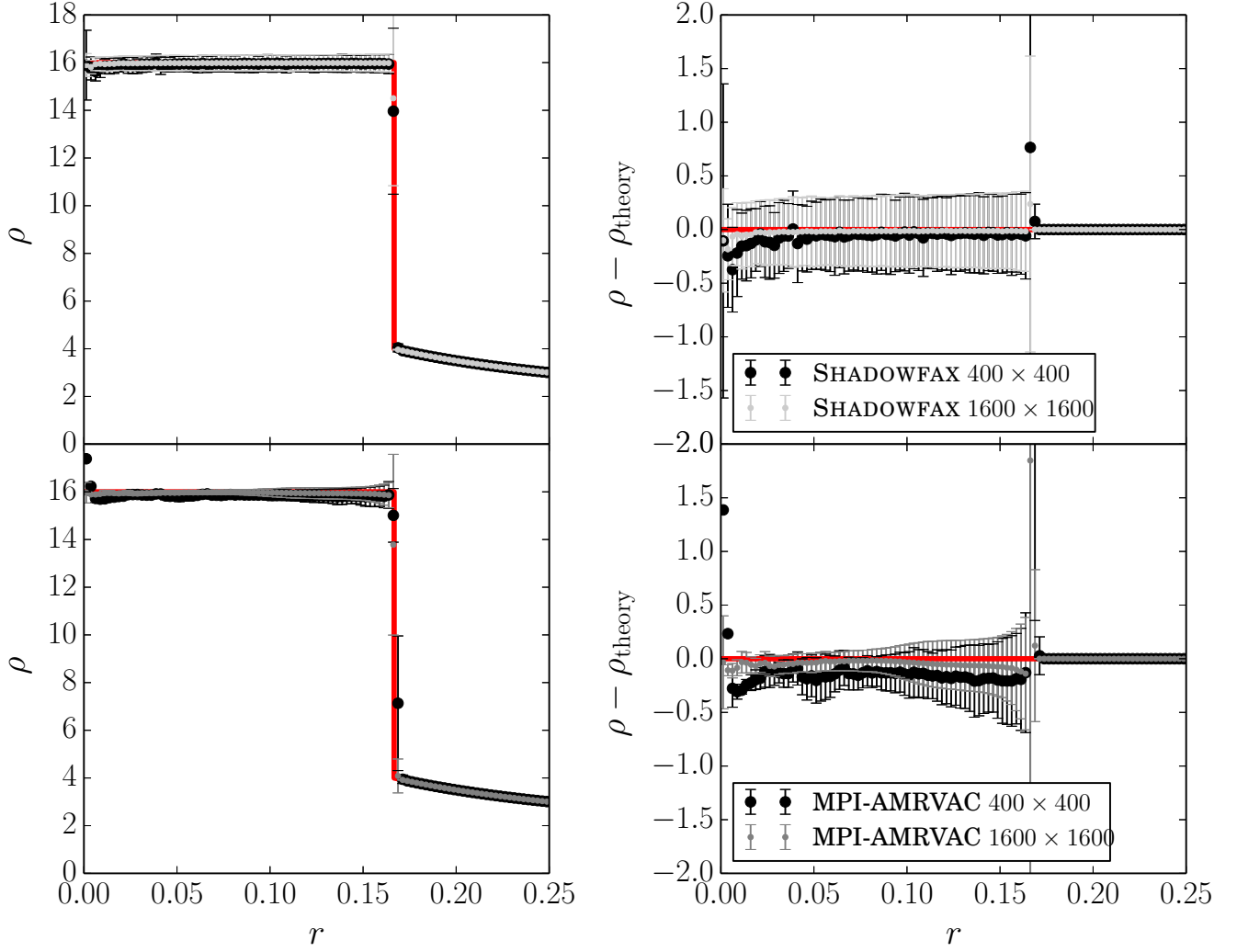


Figure 24: Radial density profile for the Noh test at $t = 0.5$. The black and gray dots show the binned density values, with the error bars indicating the standard deviation of the values inside the bins. The red line corresponds to the analytical solution. The right column shows the difference between the density and the analytical solution.

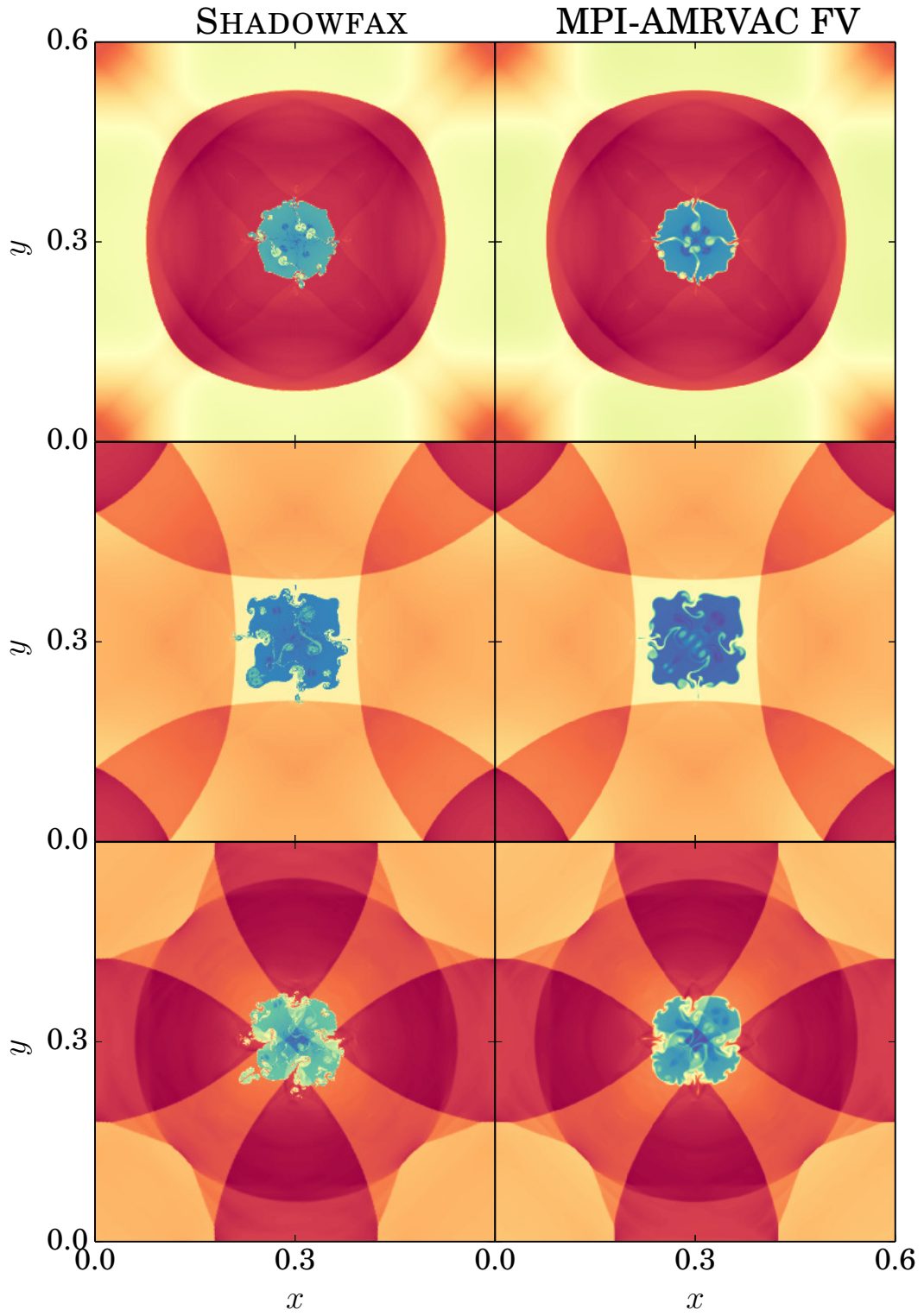


Figure 25: Density colour plots for the implosion test at different times. *Top:* $t = 0.25$, *middle:* $t = 0.5$, *bottom:* $t = 0.75$.

Acknowledgments

We thank the two anonymous referees for the constructive feedback that improved the quality of this manuscript, and for pointing out the details of our implementation we forgot to mention in the first version. We thank the Ghent University Special Research Fund and the Interuniversity Attraction Poles Programme initiated by the Belgian Science Policy Office (IAP P7/08 CHARM) for financial support. We thank Robbert Verbeke for his contribution to the exact Riemann solver, and Peter Camps for sharing the `Vec` class that originally was part of SKIRT²³ with us, before SKIRT became public. BV thanks Matthieu Schaller and Tom Theuns for the discussions about finite volume methods, and the coupling between hydrodynamics and gravity. We thank Volker Springel and Romain Teyssier for making their codes GADGET2 and RAMSES public. Special thanks also to Rony Keppens for sharing his knowledge about grid methods and helping us setting up the MPI-AMRVAC simulations. Finally, we want to thank J. R. R. Tolkien for providing an extensive list of unique names to give to computing infrastructure and simulation codes.

References

- Agertz, O., Moore, B., Stadel, J., Potter, D., Miniati, F., Read, J., Mayer, L., Gawryszczak, A., Kravtsov, A., Nordlund, Å., Pearce, F., Quilis, V., Rudd, D., Springel, V., Stone, J., Tasker, E., Teyssier, R., Wadsley, J., Walder, R., Sep. 2007. Fundamental differences between SPH and grid methods. *Mon. Not. R. Astron. Soc.* 380, 963–978.
- Barnes, J., Hut, P., Dec. 1986. A hierarchical $O(N \log N)$ force-calculation algorithm. *Nature* 324, 446–449.
- Cloet-Osselaer, A., De Rijcke, S., Vandenbroucke, B., Schroyen, J., Koleva, M., Verbeke, R., Aug. 2014. Numerical simulations of dwarf galaxy merger trees. *Mon. Not. R. Astron. Soc.* 442, 2909–2925.
- Dobbs, C. L., Mar. 2015. The interstellar medium and star formation on kpc size scales. *Mon. Not. R. Astron. Soc.* 447, 3390–3401.
- Duffell, P. C., MacFadyen, A. I., Dec. 2011. TESS: A Relativistic Hydrodynamics Code on a Moving Voronoi Mesh. *Astrophys. J. Suppl. Ser.* 197, 15.
- Duffell, P. C., MacFadyen, A. I., Aug. 2012. Global Calculations of Density Waves and Gap Formation in Protoplanetary Disks Using a Moving Mesh. *Astrophys. J.* 755, 7.
- Gaburov, E., Johansen, A., Levin, Y., Oct. 2012. Magnetically Levitating Accretion Disks around Supermassive Black Holes. *Astrophys. J.* 758, 103.
- Geen, S., Rosdahl, J., Blaizot, J., Devriendt, J., Slyz, A., Apr. 2015. A detailed study of feedback from a massive star. *Mon. Not. R. Astron. Soc.* 448, 3248–3264.
- Gonnet, P., Schaller, M., Theuns, T., Chalk, A. B. G., Sep. 2013. SWIFT: Fast algorithms for multi-resolution SPH on multi-core architectures. *ArXiv e-prints*.
- Greif, T. H., Springel, V., White, S. D. M., Glover, S. C. O., Clark, P. C., Smith, R. J., Klessen, R. S., Bromm, V., Aug. 2011. Simulations on a Moving Mesh: The Clustered Formation of Population III Protostars. *Astrophys. J.* 737, 75.
- Hendrix, T., Keppens, R., Feb. 2014. Effect of dust on Kelvin-Helmholtz instabilities. *Astron. Astrophys.* 562, A114.
- Hopkins, P. F., Jun. 2015. A new class of accurate, mesh-free hydrodynamic simulation methods. *Mon. Not. R. Astron. Soc.* 450, 53–110.
- Jin, G., Mellor-Crummey, J., Mar. 2005. Sfcgen: A framework for efficient generation of multi-dimensional space-filling curves by recursion. *ACM Trans. Math. Softw.* 31 (1), 120–148.
URL <http://doi.acm.org/10.1145/1055531.1055537>
- Keppens, R., Meliani, Z., van Marle, A., Delmont, P., Vlasov, A., van der Holst, B., 2012. Parallel, grid-adaptive approaches for relativistic hydro and magnetohydrodynamics. *J. Comput. Phys.* 231 (3), 718744, special Issue: Computational Plasma Physics Special Issue: Computational Plasma Physics.
URL <http://www.sciencedirect.com/science/article/pii/S0021999111000386>
- Lecoanet, D., McCourt, M., Quataert, E., Burns, K. J., Vasil, G. M., Oishi, J. S., Brown, B. P., Stone, J. M., O’Leary, R. M., Feb. 2016. A validated non-linear Kelvin-Helmholtz benchmark for numerical hydrodynamics. *Mon. Not. R. Astron. Soc.* 455, 4274–4288.
- Liska, R., Wendroff, B., Mar. 2003. Comparison of several difference schemes on 1d and 2d test problems for the euler equations. *SIAM J. Sci. Comput.* 25 (3), 995–1017.
URL <http://dx.doi.org/10.1137/S1064827502402120>
- Lloyd, S., Mar 1982. Least squares quantization in pcm. *EEE Trans. Inf. Theory* 28 (2), 129–137.
- Noh, W. F., Sep. 1987. Errors for calculations of strong shocks using an artificial viscosity and an artificial heat flux. *J. Comput. Phys.* 72, 78–120.
- Pakmor, R., Bauer, A., Springel, V., Dec. 2011. Magnetohydrodynamics on an unstructured moving grid. *Mon. Not. R. Astron. Soc.* 418, 1392–1401.
- Plummer, H. C., Mar. 1911. On the problem of distribution in globular star clusters. *Mon. Not. R. Astron. Soc.* 71, 460–470.
- Price, D. J., Feb. 2012. Smoothed particle hydrodynamics and magnetohydrodynamics. *J. Comput. Phys.* 231, 759–794.
- Reem, D., 2011. The geometric stability of voronoi diagrams with respect to small changes of the sites. In: *Proceedings of the Twenty-seventh Annual Symposium on Computational Geometry. SoCG ’11*. ACM, New York, NY, USA, pp. 254–263.
URL <http://doi.acm.org/10.1145/1998196.1998234>
- Richard Shewchuk, J., 1997. Adaptive Precision Floating-Point Arithmetic and Fast Robust Geometric Predicates. *Discrete Comput. Geom.* 18 (3), 305–363.
URL <http://dx.doi.org/10.1007/PL00009321>
- Schaye, J., Crain, R. A., Bower, R. G., Furlong, M., Schaller, M., Theuns, T., Dalla Vecchia, C., Frenk, C. S., McCarthy, I. G., Helly, J. C., Jenkins, A., Rosas-Guevara, Y. M., White, S. D. M., Baes, M., Booth, C. M., Camps, P., Navarro, J. F., Qu, Y., Rahmati, A., Sawala, T., Thomas, P. A., Trayford, J., 2015. The eagle project: simulating the evolution and assembly of galaxies and their environments. *Mon. Not. R. Astron. Soc.* 446 (1), 521–554.
URL <http://mnras.oxfordjournals.org/content/446/1/521.abstract>
- Sedov, L., 1977. *Similitude et dimensions en mécanique*. Edition Mir.
- Siebert, C., Wolf, F., 2010. A scalable parallel sorting algorithm using exact splitting. Tech. rep., German Research School for Simulation Sciences GmbH.
- Springel, V., Dec. 2005. The cosmological simulation code GADGET-2. *Mon. Not. R. Astron. Soc.* 364, 1105–1134.
- Springel, V., Jan. 2010. E pur si muove: Galilean-invariant cosmological hydrodynamical simulations on a moving mesh. *Mon. Not. R. Astron. Soc.* 401, 791–851.
- Sundar, H., Sampath, R. S., Biros, G., 2008. Bottom-Up Construction and 2:1 Balance Refinement of Linear Octrees in Parallel. *SIAM J. Sci. Comput.* 30 (5), 26752708.
URL <http://dx.doi.org/10.1137/070681727>
- Teyssier, R., Apr. 2002. Cosmological hydrodynamics with adaptive mesh refinement. A new high resolution code called RAMSES. *Astron. Astrophys.* 385, 337–364.
- Toro, E. F., 2009. *Riemann Solvers and Numerical Methods for Fluid Dynamics*, 3rd Edition. Springer-Verlag, Berlin Heidelberg.

²³ascl:1109.003

- Verbeke, R., Vandenbroucke, B., De Rijcke, S., Dec. 2015. How the First Stars Shaped the Faintest Gas-dominated Dwarf Galaxies. *Astrophys. J.* 815, 85.
- Vogelsberger, M., Genel, S., Springel, V., Torrey, P., Sijacki, D., Xu, D., Snyder, G., Bird, S., Nelson, D., Hernquist, L., May 2014. Properties of galaxies reproduced by a hydrodynamic simulation. *Nature* 509, 177–182.
- Vogelsberger, M., Sijacki, D., Kereš, D., Springel, V., Hernquist, L., Oct. 2012. Moving mesh cosmology: numerical techniques and global statistics. *Mon. Not. R. Astron. Soc.* 425, 3024–3057.
- Yalinewich, A., Steinberg, E., Sari, R., 2015. RICH: Open-source Hydrodynamic Simulation on a Moving Voronoi Mesh. *Astrophys. J. Suppl. Ser.* 216 (2), 35.
 URL <http://stacks.iop.org/0067-0049/216/i=2/a=35>